

# Majorana modes in graphene strips: polarization, wavefunctions, disorder, and Andreev states

Shubhanshu Karoliya,<sup>1</sup> Sumanta Tewari,<sup>2</sup> and Gargee Sharma<sup>3</sup>

<sup>1</sup>*School of Physical Sciences, Indian Institute of Technology Mandi, Mandi 175005, India.*

<sup>2</sup>*Department of Physics and Astronomy, Clemson University, Clemson, South Carolina 29634, USA.*

<sup>3</sup>*Department of Physics, Indian Institute of Technology Delhi, Hauz Khas, New Delhi 110016, India.*

Topologically protected Majorana zero modes (MZMs) have attracted intense interest due to their potential application in fault-tolerant quantum computation (TQC). Graphene nanoribbons, with tunable edge terminations and compatibility with planar device architectures, offer a promising alternative to semiconductor nanowires. Here we present a comprehensive theoretical study of finite graphene strips with armchair, zigzag, and nearly square geometries, proximitized by an s-wave superconductor and subject to Rashba spin-orbit coupling, Zeeman fields, and disorder. Using exact diagonalization of the Bogoliubov-de Gennes tight-binding Hamiltonian, we analyze Majorana polarization, low-energy spectra, and real-space wavefunctions to identify the non-trivial topological phases supporting MZMs and distinguish them from partially separated Andreev bound states (psABS) or the quasi-Majoranas. We systematically chart the robustness of these modes across geometries and disorder regimes, finding that armchair strips with short zigzag edges provide the most stable platform. Our results unify polarization diagnostics with spatial wavefunction analysis and disorder effects, yielding concrete design guidelines for graphene-based topological superconductors.

## I. INTRODUCTION

Majorana fermions (MFs), proposed as real solutions to the Dirac equation [1], remain elusive as fundamental particles despite ongoing high-energy physics searches [2]. In condensed matter, however, MFs can arise as zero-energy quasiparticles in certain superconductors, where they exhibit non-Abelian exchange statistics [3–5], and offer a potential route towards fault-tolerant topological quantum computation (TQC) [6, 7]. The canonical platform for realizing such states employs a spin-orbit coupled semiconductor proximitized by an s-wave superconductor under a Zeeman field [8–11], which supports topological Majorana bound states (MBSs) localized at the boundaries of the system. The Rashba spin-orbit coupled one-dimensional nanowire is the most widely studied realization of this proposal. In the topological regime, MBSs are predicted to generate a quantized zero-bias conductance peak of  $2e^2/h$  in tunneling spectroscopy [12–14], robust to variations in magnetic field and gate voltage. While numerous experiments have reported features consistent with this picture [15–39], similar zero-bias signatures can also emerge from topologically trivial states [40–60], such as partially separated Andreev bound states (psABSs) [46, 47] stabilized by disorder. This ambiguity has motivated the search for complementary diagnostics and alternative material platforms.

Graphene has emerged as a particularly attractive candidate. While pristine graphene is gapless and exhibits negligible intrinsic spin-orbit coupling, engineering finite-width graphene nanoribbons (GNRs) in proximity to an s-wave superconductor can open a superconducting gap and enable topological phases when Rashba spin-orbit coupling (RSOC) and a Zeeman field are introduced. Such graphene-superconductor hybrids combine experimental tunability with planar scalability, and several

works have analyzed Majorana bound states in graphene nanoribbons and flakes [61–67]. In parallel, Majorana polarization (MP) has been proposed as a powerful diagnostic tool for distinguishing MZMs from trivial modes [68–71]. Yet, most studies have focused either on polarization diagnostics in idealized systems or on graphene wavefunctions in the clean limit, without a unified analysis of polarization diagnostics, disorder robustness, and possible competing Andreev-bound-state physics. Thus there remains a critical gap: a comprehensive, self-consistent treatment that combines (i) Majorana polarization, (ii) real-space wavefunction morphology, (iii) disorder effects, and (iv) analysis of psABS (quasi-Majoranas) and Andreev bound states, all within the graphene geometry context, is largely missing from the literature. This is especially important because graphene’s two-dimensional nature, edge types (zigzag, armchair), and richer band-structure nuances imply that simplistic extrapolations from nanowires may fail.

In this work we address this gap. We perform a systematic investigation of finite-size graphene strips with different edge terminations: armchair, zigzag, and nearly square geometries, proximitized by an s-wave superconductor, subject to Rashba spin-orbit coupling and both in-plane and out-of-plane magnetic fields. Using exact diagonalization of the BdG Hamiltonian, we compute phase diagrams of MP, track bulk gap closings/reopenings, and image real-space localization for low-energy modes in clean and disordered regimes. By cross-correlating MP with wavefunction localization and monitoring psABS proliferation, we establish practical criteria for distinguishing genuine MZMs from trivial near-zero modes. Our analysis shows that the combination of edge geometry, magnetic field orientation, and disorder strength plays a decisive role in accessing and stabilizing topological superconducting phases supporting Majorana zero modes. We show that armchair strips

with short zigzag ends best support sharply localized, well-separated MZMs that remain stable under moderate disorder; by contrast, zigzag and square geometries display narrower windows and are more easily compromised by disorder-induced psABSs. Our analysis provides not only a consistency check across multiple diagnostics but also design principles for scalable graphene-based platforms.

The remainder of this paper is organized as follows. In Sec. II, we introduce the tight-binding model for a graphene-based system with proximity-induced superconductivity, mapped onto an effective  $p$ -wave superconductor. Section III reviews the concept of Majorana polarization, including both the chiral-symmetry-based formulation [68] and the more general definition applicable to systems in which chiral symmetry is absent [69]. Section IV describes the finite-size graphene geometries considered in this work. In Sec. V, we present our results for Majorana zero modes in the three geometries, analyzing the role of magnetic field orientation, the importance of edge termination, and disorder strength. Finally, Sec. VI summarizes our conclusions.

## II. MODEL

We model graphene strips with proximity-induced superconductivity with the following tightbinding Hamiltonian [62]:

$$H_0 = \sum_j \Psi_j^\dagger [V(\mathbf{x}_j)\tau^z - \mu\tau^z - \Delta\tau^x] \Psi_j - t \sum_{\langle i,j \rangle} \Psi_i^\dagger \tau^z \Psi_j \quad (1)$$

The above Hamiltonian is written in a four-component Nambu basis,  $\Psi_j = (c_{j,\uparrow}, c_{j,\downarrow}, c_{j,\downarrow}^\dagger, -c_{j,\uparrow}^\dagger)^T$ . Here  $c_{j,\sigma}^\dagger$  creates an electron with spin  $\sigma$  at the site  $j$ . We use Pauli matrices,  $\vec{\tau} = (\tau_x, \tau_y, \tau_z)$  for the particle-hole subspace, and  $\vec{\sigma} = (\sigma_x, \sigma_y, \sigma_z)$  for the spin subspace. In the above equation,  $\tau^k \equiv \tau_k \otimes \sigma_0$  where  $k = x, y, z$ ;  $t$  denotes the hopping strength,  $\mu$  represents the chemical potential,  $V(\mathbf{x}_j)$  represents the position dependent potential, and  $\Delta$  is the induced superconducting pairing potential. The summation  $\langle i, j \rangle$  is restricted to only the nearest neighbors. Unless otherwise specified, throughout this manuscript, all the energy scales are expressed in terms of the hopping strength  $t$ , and all the distances are expressed in terms of the nearest-neighbor distance  $a$ .

The next term in the Hamiltonian describes the effect of the Zeeman magnetic field  $\vec{h}$ , expressed as:

$$H_B = \sum_j \Psi_j^\dagger \vec{h} \cdot \vec{\sigma} \Psi_j, \quad (2)$$

where  $\vec{h} \cdot \vec{\sigma} \equiv h_k \tau_0 \otimes \sigma_k$  for  $k = x, y, z$ . Throughout this work we retain only the Zeeman coupling of the magnetic field and neglect its orbital effect. For in-plane magnetic

fields, this approximation is well justified, since an external field parallel to the graphene sheet produces negligible magnetic flux through the monolayer and therefore induces no significant orbital coupling. In contrast, a perpendicular magnetic field would generate Landau quantization and strong orbital effects; hence, in the out-of-plane case, the Zeeman term is understood to arise from magnetic proximity to a ferromagnetic insulator rather than from an externally applied field. Such an exchange-induced Zeeman field acts only on the electron spin and does not generate a vector potential in graphene, thereby allowing us to include the Zeeman splitting without introducing orbital couplings in the tight-binding model. The third term,  $H_R$ , accounts for the effective Rashba spin-orbit interaction of strength  $\alpha$ , and is given by:

$$H_R = i\alpha \sum_{\langle i,j \rangle} \Psi_i^\dagger (\vec{\delta}_{ij} \times \vec{\sigma}) \cdot \hat{z} \tau^z \Psi_j \quad (3)$$

The complete Hamiltonian is thus expressed as:

$$H = H_0 + H_R + H_B. \quad (4)$$

In our calculations, unless otherwise specified, we fix  $\alpha = 0.5t$ ,  $\Delta = 0.2t$ .  $V(\mathbf{x}_i)$  is the effective position-dependent disorder potential, which is modeled by considering  $N_d$  randomly distributed short-range impurities. The potential profile of an isolated impurity located at position  $\mathbf{x}_i$  is

$$V_{\text{imp}}^{(i)}(\mathbf{x}) = A_i \exp\left(-\frac{|\mathbf{x} - \mathbf{x}_i|}{\lambda}\right), \quad (5)$$

where  $\lambda$  is the characteristic decay length of the impurity potential and  $A_i$  is a random amplitude characterized by a Gaussian probability distribution. The net disorder potential at position  $\mathbf{x}$  is then given by

$$V(\mathbf{x}) = V_0 \sum_{i=1}^{N_d} A_i \exp\left(-\frac{|\mathbf{x} - \mathbf{x}_i|}{\lambda}\right), \quad (6)$$

where  $V_0$  allows us to tune the overall magnitude of the disorder for a given disorder configuration.

## III. MAJORANA POLARIZATION IN GRAPHENE STRIPS

Before we proceed to discuss the geometry-dependent behavior of Majorana modes in graphene nanoribbons, we discuss the definitions of Majorana polarization that are applicable to Graphene. Graphene has a bipartite lattice structure composed of A and B sublattices. In the following Nambu basis:

$$(c_{iA\uparrow}^\dagger, c_{iB\uparrow}^\dagger, c_{iA\downarrow}^\dagger, c_{iB\downarrow}^\dagger, c_{iA\downarrow}, c_{iB\downarrow}, -c_{iA\uparrow}, -c_{iB\uparrow}),$$

where  $i$  labels the lattice site, let us suppose that the solution of the BdG Hamiltonian at energy  $\epsilon$  is

$$\psi_i(\epsilon) = (u_{iA\uparrow}, u_{iB\uparrow}, u_{iA\downarrow}, u_{iB\downarrow}, v_{iA\downarrow}, v_{iB\downarrow}, v_{iA\uparrow}, v_{iB\uparrow}),$$

where  $u_{i\alpha}$  and  $v_{i\alpha}$  are particle and hole components for the  $\alpha$  sublattice. Due to particle-hole symmetry, a corresponding eigenstate exists at  $-\epsilon$ , given by

$$\psi_i(-\epsilon) = (v_{iA\uparrow}^*, v_{iB\uparrow}^*, v_{iA\downarrow}^*, v_{iB\downarrow}^*, u_{iA\downarrow}^*, u_{iB\downarrow}^*, u_{iA\uparrow}^*, u_{iB\uparrow}^*).$$

We define a Majorana basis as:

$$\begin{aligned} \gamma_{i\alpha\sigma}^1 &= \frac{1}{\sqrt{2}} (c_{i\alpha\sigma}^\dagger + c_{i\alpha\sigma}), \\ \gamma_{i\alpha\sigma}^2 &= \frac{i}{\sqrt{2}} (c_{i\alpha\sigma}^\dagger - c_{i\alpha\sigma}), \end{aligned} \quad (7)$$

where  $\alpha$  is the sublattice index. The Majorana polarization on the A sublattice at site  $i$  is defined as the difference in probabilities for the two Majorana components  $\gamma_{iA\sigma}^1$  and  $\gamma_{iA\sigma}^2$ . Analogously, for the B sublattice at site  $j$ , we compute the difference between  $\gamma_{iB\sigma}^1$  and  $\gamma_{iB\sigma}^2$ . The rationale behind this is that the sum of probabilities corresponds to a full fermionic state, while the difference corresponds to a Majorana state. Using the above basis, the polarization becomes [68]:

$$\mathcal{P}_i^\alpha = 2 \operatorname{Re} [u_{i\alpha\downarrow} v_{i\alpha\downarrow}^* - u_{i\alpha\uparrow} v_{i\alpha\uparrow}^*].$$

The local Majorana polarization at a given site on sublattice  $\alpha$  and energy  $\omega$  is defined as:

$$\mathcal{P}_i^\alpha(\omega) = 2 \sum_k \delta(\omega - \epsilon_k) \operatorname{Re} [u_{i\alpha\downarrow}^k v_{i\alpha\downarrow}^{k*} - u_{i\alpha\uparrow}^k v_{i\alpha\uparrow}^{k*}], \quad (8)$$

where the summation runs over all eigenstates of the Bogoliubov-de Gennes (BdG) Hamiltonian, and  $u_{i\alpha\sigma}^k, v_{i\alpha\sigma}^k$  are the particle and hole components of the  $k$ -th eigenstate at site  $i$  with sublattice  $\alpha$ , and spin  $\sigma$ . One may then sum over a suitable region  $\mathcal{R}$  and calculate the total polarization in the region. This definition of MP works well if the Hamiltonian preserves chiral symmetry, i.e., the A and B sublattices *do not see* each other. If chiral symmetry is broken, for example by a transverse Rashba term [72], then the Majorana modes localized at A and B sublattices may couple to one other and thus it is useful to employ a general definition of Majorana polarization.

In a recent work, Sedlmayr *et al.* [69] introduced a general definition of Majorana polarization valid in systems with or without chiral symmetry. The Bogoliubov-de Gennes Hamiltonian ( $H_{\text{BdG}}$ ), which describes excitations of a superconductor, inherently has built-in particle-hole symmetry. This symmetry operation is represented by a particle-hole operator  $\mathcal{C}$  that anticommutes with the  $H_{\text{BdG}}$ . Since a true Majorana bound state,  $|\psi\rangle$ , is an equal superposition of both particle and hole components, it is an eigenstate of both the Hamiltonian  $H_{\text{BdG}}$

and the particle-hole operator  $\mathcal{C}$ , and therefore must occur at exactly zero energy, i.e.,  $([H_{\text{BdG}}, \mathcal{C}]_\pm |\psi\rangle) = 0$ , where  $\pm$  refer to commutator/anti-commutator). The particle-hole operator takes the form  $\mathcal{C} = \nu_0 \sigma_y \tau_y \mathcal{K}$ , where  $\sigma_y$  and  $\tau_y$  are Pauli- $y$  matrices for spin and electron-hole degree of freedoms,  $\nu_0$  acts on the sublattice degree of freedom, and  $\mathcal{K}$  represents complex conjugation. The local Majorana polarization  $\mathcal{P}(\mathbf{r}_i, \epsilon)$  at a particular site  $\mathbf{r}_i$  is defined to be the expectation value of the particle hole operator, i.e.,  $\mathcal{P}(\mathbf{r}_i, \epsilon_j) = \langle \psi(\mathbf{r}_i, \epsilon_j) | \mathcal{C} | \psi(\mathbf{r}_i, \epsilon_j) \rangle$ . Furthermore, if an MBS is localized in a region  $\mathcal{R}$  in space, the normalized polarization should be a complex number with unit magnitude, i.e.,

$$\mathcal{P}_{\mathcal{R}}(\epsilon_j) = \frac{\sum_{i \in \mathcal{R}} \langle \psi(\mathbf{r}_i, \epsilon_j) | \mathcal{C} | \psi(\mathbf{r}_i, \epsilon_j) \rangle}{\sum_{i \in \mathcal{R}} \langle \psi(\mathbf{r}_i, \epsilon_j) | \psi(\mathbf{r}_i, \epsilon_j) \rangle} = e^{i\xi}. \quad (9)$$

To evaluate the polarization at a finite frequency  $\omega$  we sum over the eigenstates weighted by a Dirac-delta function, i.e.,

$$\mathcal{P}_{\mathcal{R}}(\omega) = \sum_j \left[ \frac{\sum_{i \in \mathcal{R}} \langle \psi(\mathbf{r}_i, \epsilon_j) | \mathcal{C} | \psi(\mathbf{r}_i, \epsilon_j) \rangle}{\sum_{i \in \mathcal{R}} \langle \psi(\mathbf{r}_i, \epsilon_j) | \psi(\mathbf{r}_i, \epsilon_j) \rangle} \right] \cdot \delta(\epsilon_j - \omega) \quad (10)$$

Here, the summation  $j$  is over all the eigenstates, and the Dirac-Delta function is implemented by a narrow Gaussian factor of width  $\sigma$ . Note that  $\mathcal{P}_{\mathcal{R}}$  is a complex number, with real and imaginary parts,  $\mathcal{P}_{\mathcal{R}} = \mathcal{P}_{\mathcal{R}}^x + i\mathcal{P}_{\mathcal{R}}^y$ . Reference [73] recently introduced the quantity  $\mathcal{P}_l^* \mathcal{P}_r$  as a measure for identifying non-local correlations between the two halves of a system. While  $\mathcal{P}_l$  and  $\mathcal{P}_r$  are individually complex, their conjugate product,  $P = \mathcal{P}_l^* \mathcal{P}_r = \mathcal{P}_l \mathcal{P}_r^*$ , was found to be real in that work. In our earlier study of one-dimensional nanowires and quasi-1D systems [71], we also observed  $P$  to be real. However, in our recent investigation of a finite-size graphene strip platform for Majorana modes, we find that  $P$  is generally complex. Consequently, we use  $|P|$  as a diagnostic tool for Majorana mode identification, [69].

Before analyzing the geometry and topological properties of the finite-size graphene nanoribbon, it is useful to clarify how the fermion-doubling constraints of lattice Dirac systems apply to our model. The fermion-doubling problem is a generic artifact of lattice regularizations of massless chiral fermions, under very general assumptions of locality, Hermiticity, and discrete translational invariance [74–77]. In pristine graphene, this doubling is realized as the well-known valley degeneracy: the honeycomb lattice supports two inequivalent Dirac cones at the K and K' points, which are related by lattice symmetries and carry opposite Berry-phase winding, so that the low-energy theory consists of two species of massless Dirac fermions. In the proximitized graphene nanoribbon considered here, this bulk doubling is rendered irrelevant for the Majorana physics in two steps: (i) first, the finite-size graphene strip imposes boundary conditions that explicitly admix K and K' valley components

of the wavefunction, lifting valley as a good quantum number and producing a single ladder of transverse 1D subbands rather than two independent valley copies [78], (ii) second, the Rashba spin-orbit coupling, a uniform Zeeman field, and proximity-induced s-wave pairing lift the residual spin degeneracy so that, for suitable values of chemical potential ( $\mu/t$ ) and Zeeman energy ( $h/t$ ), only one helical subband crosses the Fermi level. The presence of disorder further breaks translational invariance along the ribbon, so the conditions of the Nielsen-Ninomiya theorem are not satisfied, and no additional low-energy doublers are enforced.

#### IV. GRAPHENE GEOMETRIES

Graphene in the bulk respects time-reversal, inversion, and threefold rotational symmetry ( $C_3$ ), which together protect the local and global stability of its Dirac points [79]. In contrast, finite-size realizations such as nanoribbons and flakes break some of these symmetries and display rich boundary physics, including edge-localized states and geometry-dependent spectral gaps. A key distinction arises from the termination: zigzag edges naturally host states pinned near zero energy, while armchair edges do not. When graphene is proximitized by an s-wave superconductor in addition to Rashba spin-orbit coupling and a Zeeman field, the nature of its edges plays a decisive role in shaping zero-energy Majorana bound states. We find that the stability of Majorana-supporting topological phases is not universal to all proximitized graphene structures, but depends critically on the edge termination and the orientation of the applied field. This aspect will be explored in detail in the following sections.

Finite-size graphene strips are formed by cutting a graphene sheet along specific crystallographic directions [80–83]. Fig. 1 (a) illustrates a finite-size armchair graphene strip with  $N = 5$  and  $L = 15$  (A-strip), (b) zigzag strip with  $N = 21$  and  $L = 3$  (Z-strip), (c) square strip  $N = 12$  and  $L = 5$  (S-strip) where  $N$  denotes the layer index and  $L$  represents the unit cell. Note that the the actual system size we consider in our study is much larger. Specifically, we analyze three representative geometries: a Z-strip with  $N = 171$  and  $L = 3$ , an A-strip with  $N = 3$  and  $L = 171$ , and an S-strip with  $N = 35$  and  $L = 15$ . In each case, the total number of lattice sites is  $N \times (2L)$ . Throughout this work, the strips are oriented such that the armchair edge lies along the  $x$  direction.

#### V. MAJORANA ZERO MODES IN GRAPHENE STRIPS

Majorana zero modes useful for topological quantum computation are distinguished by the following features: (a) zero-energy protected by the superconducting spectral gap, (b) a non-zero Majorana polarization, and (c)

localized wave functions at the edges or ends of the graphene strip. In the following subsections, we investigate topological superconductivity in graphene strips with armchair, zigzag, and square geometries. True Majorana modes are identified using the three criteria outlined above, after which we examine how disorder modifies their stability. To assess robustness, we consider three disorder regimes: (i) weak disorder with 20 impurities ( $\mathcal{Z} = 20$ ) and  $V_0 = 1.0$ , (ii) moderate disorder with 50 impurities ( $\mathcal{Z} = 50$ ) and  $V_0 = 1.0$ , and (iii) strong disorder with 150 impurities ( $\mathcal{Z} = 150$ ) and  $V_0 = 1.5$ . Representative spatial profiles of the disorder potential are shown in Fig. 2. In contrast to the simple one-dimensional nanowire, where the criterion  $h > \sqrt{\mu^2 + \Delta^2}$  sharply defines the topological region, the corresponding phase structure in finite graphene strips is more intricate, non-universal, and geometry-dependent. Furthermore, multiple overlapping polarization triangles are observed in the phase diagram as  $h$  and  $\mu$  are varied, which is a generic feature of multiband systems [62, 63, 69, 70]. As the bandstructure varies upon changing parameters, one or more bands cuts across the chemical potential causing the appearance and disappearance of topologically protected Majorana bound states.

##### A. Armchair

In this subsection, we examine the system the A-type (armchair) graphene strip. For our calculations, the strip dimensions are chosen as  $N = 3$  and  $L = 171$ , with an in-plane magnetic field applied along the  $x$ -direction, i.e., along the longer direction. The results are presented in Fig. 3 in three panels ((a), (b), and (c)), with a set of four figures each, labeled (i)-(iv), corresponding to different disorder strengths: (i) a clean system, (ii) a weakly disordered system with 20 impurities and  $V_0 = 1.0$ , (iii) a moderately disordered system with 50 impurities and  $V_0 = 1.0$ , and (iv) a strongly disordered system with 150 impurities and  $V_0 = 1.5$ . Each panel gives following information: (a) the phase diagram showing the Majorana polarization as a function of Zeeman field  $h_x$  and chemical potential  $\mu$ ; (b) the energy spectrum, where the lowest 100 eigenvalues are plotted as a function of  $h_x$  for a fixed  $\mu$ ; and (c) the Majorana polarization  $|\mathcal{P}^\nu|$  (with  $\nu = u, d, l, r$ ), plotted as a function of  $h_x$  for the same value of  $\mu$ . To compute  $|\mathcal{P}^\nu|$ , we define the region  $\mathcal{R}$  [9] as comprising the upper half (u), lower half (d), left half (l), and right half (r) of the strip. The polarization  $|\mathcal{P}^\nu|$  is obtained by summing the weighted contributions from the lowest 100 eigenmodes, within each spatial region. In our results, we find that  $|\mathcal{P}^u|$ ,  $|\mathcal{P}^d|$ ,  $|\mathcal{P}^l|$ , and  $|\mathcal{P}^r|$  exhibit nearly same values. Therefore, for clarity and simplicity, only  $|\mathcal{P}^d|$  is shown in the phase plots for all cases.

Fig. 3 (a), shows that regions with non-zero Majorana polarization appear as prominent “band-like” structures. Note that the background with  $\mathcal{P}^d$  is shaded gray to better highlight regions with non-zero polarization. As the



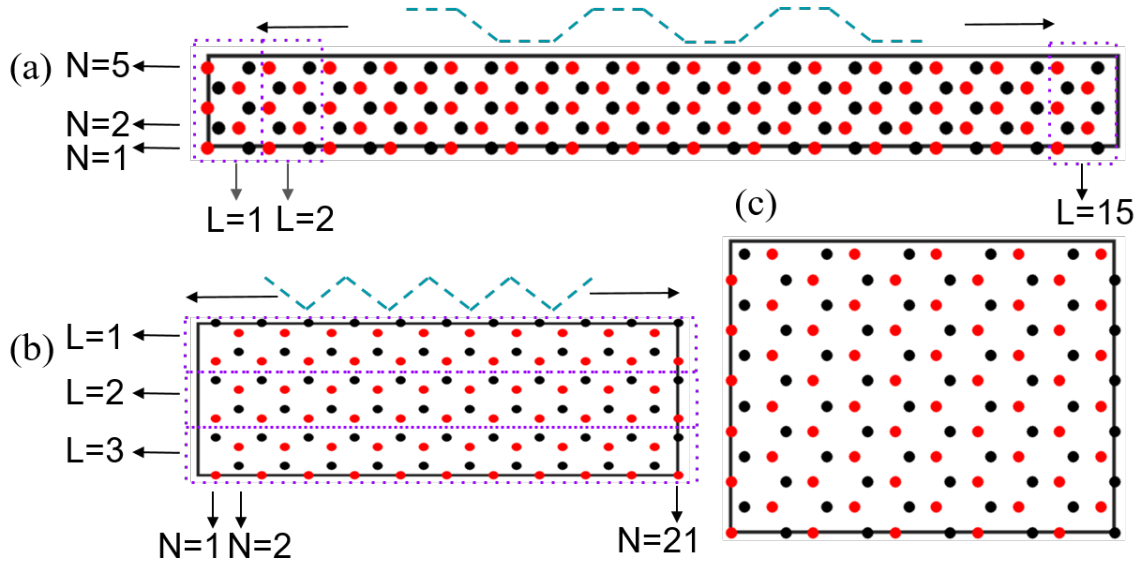


Figure 1. A finite-size graphene strip of various geometries. (a) Armchair type strip (A-strip) with  $N = 5$  and  $L = 15$  (zigzag short edges). (b) Zigzag type strip (Z-type) with  $N = 21$  and  $L = 3$  (armchair short edges). (c) Nearly square type strip (S-type) with  $N = 12$  and  $L = 5$ .  $N$  represents the number of layers, and  $L$  represents the number of unit cells in a system. Red and black dots denote the sublattices.

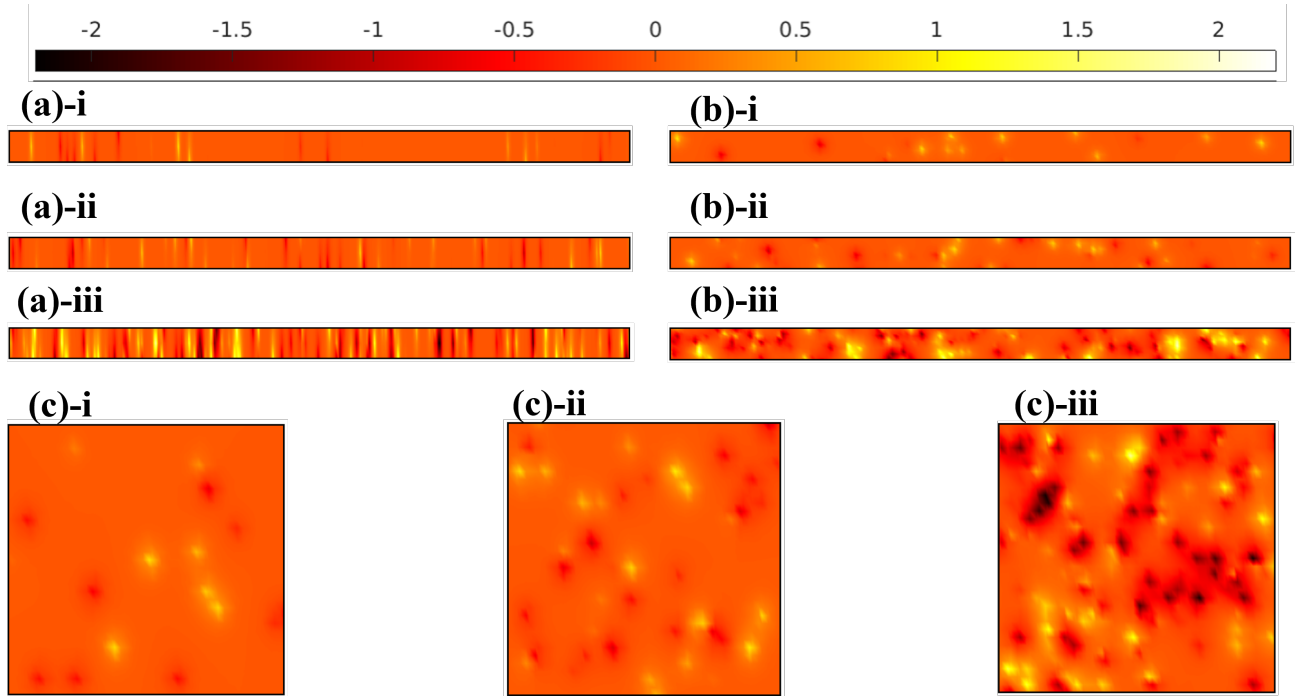


Figure 2. Spatial profiles of disorder potentials used in our calculations for different ribbon geometries: (a) armchair strip, (b) zigzag strip, and (c) square strip. Panels (i), (ii), and (iii) correspond to increasing disorder strengths: weak disorder with  $\mathcal{Z} = 20$  impurities and  $V_0 = 1.0$  (top row), moderate disorder with  $\mathcal{Z} = 50$  impurities and  $V_0 = 1.0$  (middle row), and strong disorder with  $\mathcal{Z} = 150$  impurities and  $V_0 = 1.5$  (bottom row). The color scale represents the disorder potential values, ranging from  $-2.2$  to  $+2.2$ .

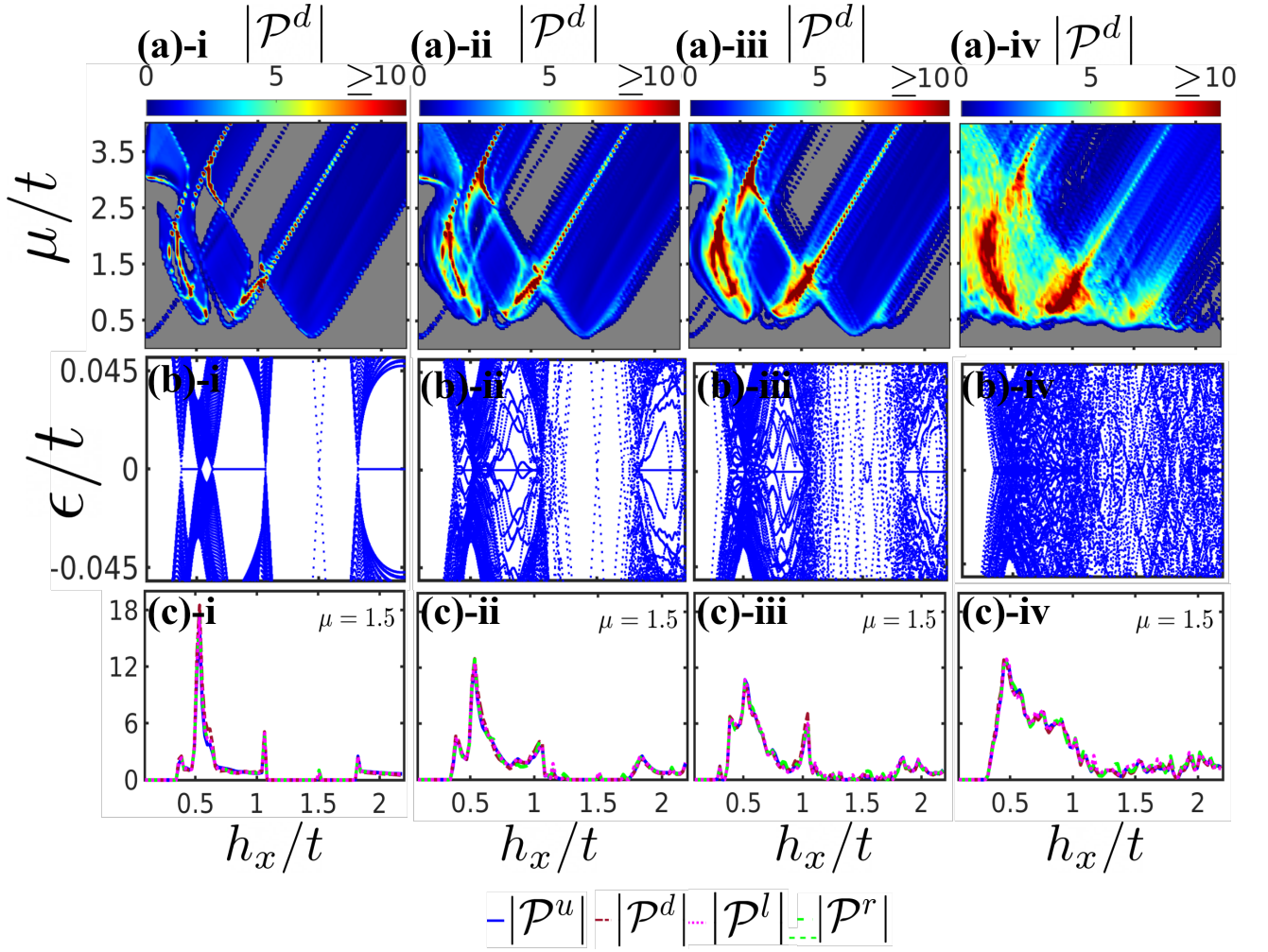


Figure 3. Majorana polarization in a finite-size **armchair** graphene strip. Each column (i-iv) corresponds to a different disorder strength: (i) clean system (no disorder), (ii) weak disorder ( $Z = 20$ ), 20 impurities,  $V_0 = 1.0$ , (iii) moderate disorder ( $Z = 50$ ), 50 impurities,  $V_0 = 1.0$ , (iv) strong disorder ( $Z = 150$ ), 150 impurities,  $V_0 = 1.5$ . Panels: (a) Heatmap of the absolute value of Majorana polarization in the lower half of the strip,  $|\mathcal{P}^d|$ , as a function of Zeeman energy ( $h_x/t$ ) and chemical potential ( $\mu/t$ ). (b) Energy spectrum as a function of  $h_x/t$  at fixed chemical potential  $\mu = 1.5$ . (c) Absolute value of Majorana polarization  $|\mathcal{P}^\nu|$  with  $\nu = u, d, l, r$  (upper, lower, left, right halves) as a function of  $h_x/t$ , also at  $\mu = 1.5$ .

disorder strength increases from (a-i) to (a-iv), these regions broaden and eventually diffuse under strong disorder, indicating the breakdown of the topological phase. In panel (b), which presents the energy spectrum, we fix the chemical potential and plot the lowest 100 eigenvalues as a function of the Zeeman field  $h_x$ . For the clean system [Fig. 3(b-i)], clear band openings and closings are observed. Specifically, three distinct regions appear where zero-energy modes coexist with a finite spectral gap, which is a necessary, though not sufficient, condition for the presence of topologically protected Majorana modes. In the disordered cases, we observe that increasing disorder leads to the accumulation of low-energy states near zero energy. At high disorder [Fig. 3(b-iv)], the gap completely closes, indicating the absence of a topological phase. Up to moderate disorder, however, zero-energy states persist within partially open bands.

To determine which of these regions correspond to genuine topological phases, we examine the Majorana polarization plots in the third panel, where  $\mathcal{P}^\nu$ 's are shown as a function of  $h_x$  at  $\mu = 1.5$  and wavefunction plots in the Fig. 4. It is worth noting that sharp peaks in the Majorana polarization in Fig. 3(c) are typically associated with closing and reopening of the bulk gap, signaling topological phase transitions.

We next turn to the spatial profiles of the wave functions, obtained by constructing a weighted superposition of the low-energy eigenstates, in the A-type (armchair) geometry. We observe a variety of localization behaviors, such as: (i) states localized at both ends of the strip, (ii) states localized only at a single end of the strip, (iii) states extended throughout the strip, (iv) states localized at intermediate positions on the strip away from the ends. In the wavefunction plots (Fig. 4), the labels (a),

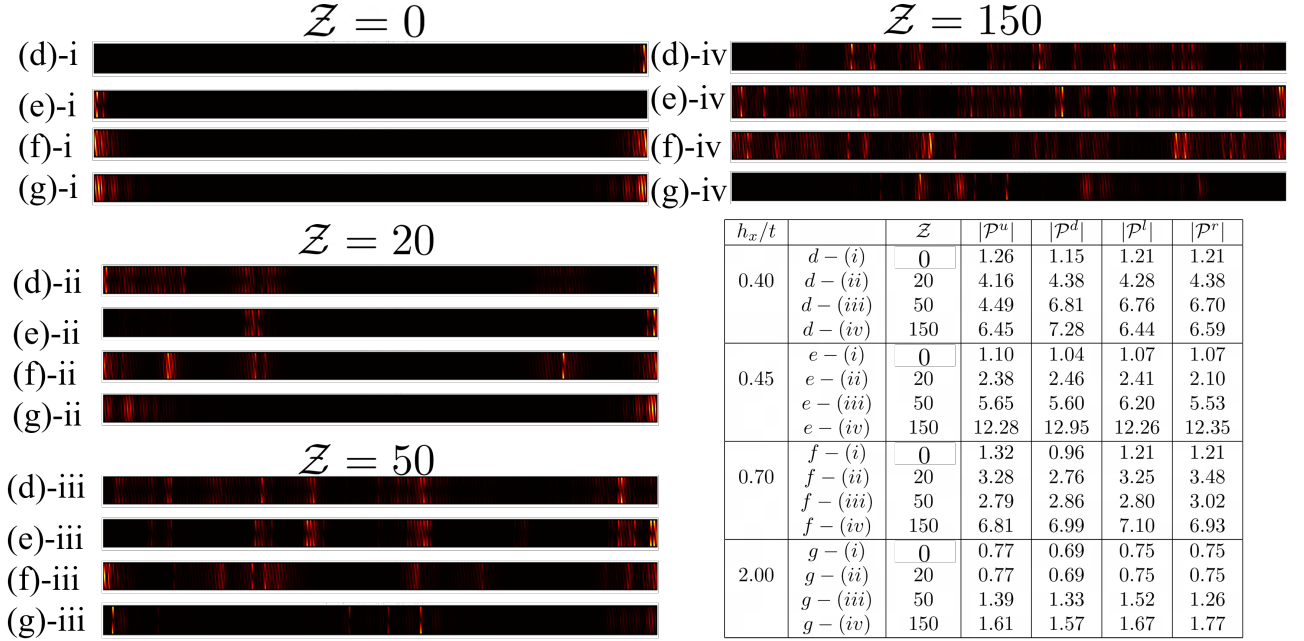


Figure 4. Real-space probability distribution of the low-energy Majorana modes on an **armchair** graphene nanoribbon under varying magnetic field and disorder strength. Panels (d)-(g) correspond to increasing values of Zeeman field  $h_x/t = 0.40, 0.45, 0.70$ , and  $2.0$ , respectively, at fixed chemical potential  $\mu/t = 1.5$ . Each row (i-iv) shows the effect of increasing disorder strength: (i) Clean (no disorder), (ii) Weak disorder ( $\mathcal{Z} = 20$ ,  $V_0 = 1.0$ ), (iii) Moderate disorder ( $\mathcal{Z} = 50$ ,  $V_0 = 1.0$ ), and (iv) Strong disorder ( $\mathcal{Z} = 150$ ,  $V_0 = 1.5$ ). The adjacent table presents the absolute value of the Majorana polarization  $|\mathcal{P}|$  for the lower ( $\mathcal{P}^d$ ), upper ( $\mathcal{P}^u$ ), left ( $\mathcal{P}^l$ ), and right ( $\mathcal{P}^r$ ) halves of the strip for each case.

(b), (c), etc., correspond to different values of the magnetic field  $h_x/t$ , while the sub-labels (i) - (iv) represent the increasing strength of the disorder: clean ( $\mathcal{Z} = 0$ ), weak ( $\mathcal{Z} = 20$ ), moderate ( $\mathcal{Z} = 50$ ), and strong disorder ( $\mathcal{Z} = 150$ ), respectively. Noting the spectrum in Fig. 3 (b)-i, we identify three regions or *phases* in  $h_x/t$  where zero energy states appear with the spectral gap: (i)  $h_x/t \approx 0.3-0.5$ , (ii)  $h_x/t \approx 0.55-1.0$ , and (iii)  $h_x/t \gtrsim 1.8$ . We select representative values from each region to examine their wavefunction characteristics.

*phase-(i):* In Fig. 4, panels (d) and (e) correspond to  $h_x/t = 0.40$  and  $0.45$ , respectively, both from the first phase. The wavefunctions in (d)-i and (e)-i are localized at only one edge of the strip, indicating that these zero-energy modes are topologically trivial. The role of disorder further supports this inference. In the low-energy spectra [Fig. 3(b)-ii, iii, iv], the first phase is no longer distinguishable as disorder increases; the corresponding zero-energy states merge into a continuum of low-energy modes, closing the bandgap necessary for topological protection. The associated wavefunctions [Fig. 4(d)-ii-iv and (e)-ii-iv] lose their edge localization and become randomly distributed within the bulk of the strip, which suggests their trivial nature.

*phase-(ii) and (iii):* We next consider  $h_x/t$  values from the second and third regions. In Fig. 4(f)-i and (g)-i, corresponding to these phases, the wavefunctions are sharply localized at the zigzag (shorter) edges. To eval-

uate their robustness, we analyze both the low-energy spectra [Fig. 3(b)-ii-iv] and the wavefunctions [Fig. 4(f)-ii-iii and (g)-ii-iii]. We find that these edge-localized modes enjoy gap-protection under weak and moderate disorder, although some additional bulk weight starts to appear with increasing disorder strength. Under strong disorder, however, the edge localization is lost, and the zero-energy modes vanish. These observations indicate that the second and third phases are topological in nature and can support robust Majorana zero modes, at least up to moderate levels of disorder. The table in the Fig. 4 has an absolute value for the left-, right-, upper-, and lower-half Majorana polarization values.

## B. Zigzag

Here we examine the system with a Z-type (zigzag) graphene strip. To ensure the total number of lattice sites matches that of the A-type strip, we set the strip dimensions to  $N = 171$  and  $L = 3$ . An in-plane magnetic field is applied along the  $y$ -direction, which is in the direction of the longer (zigzag) edge. The phase diagrams in Z-type strip shown in Fig. 5(a) exhibit a different structure compared to the the A-type strip shown in Fig. 3(a). For the Z-strip, we observe multiple sharp, V-shaped valley patterns formed by overlapping triangular regions, which can be contrasted to the A-type

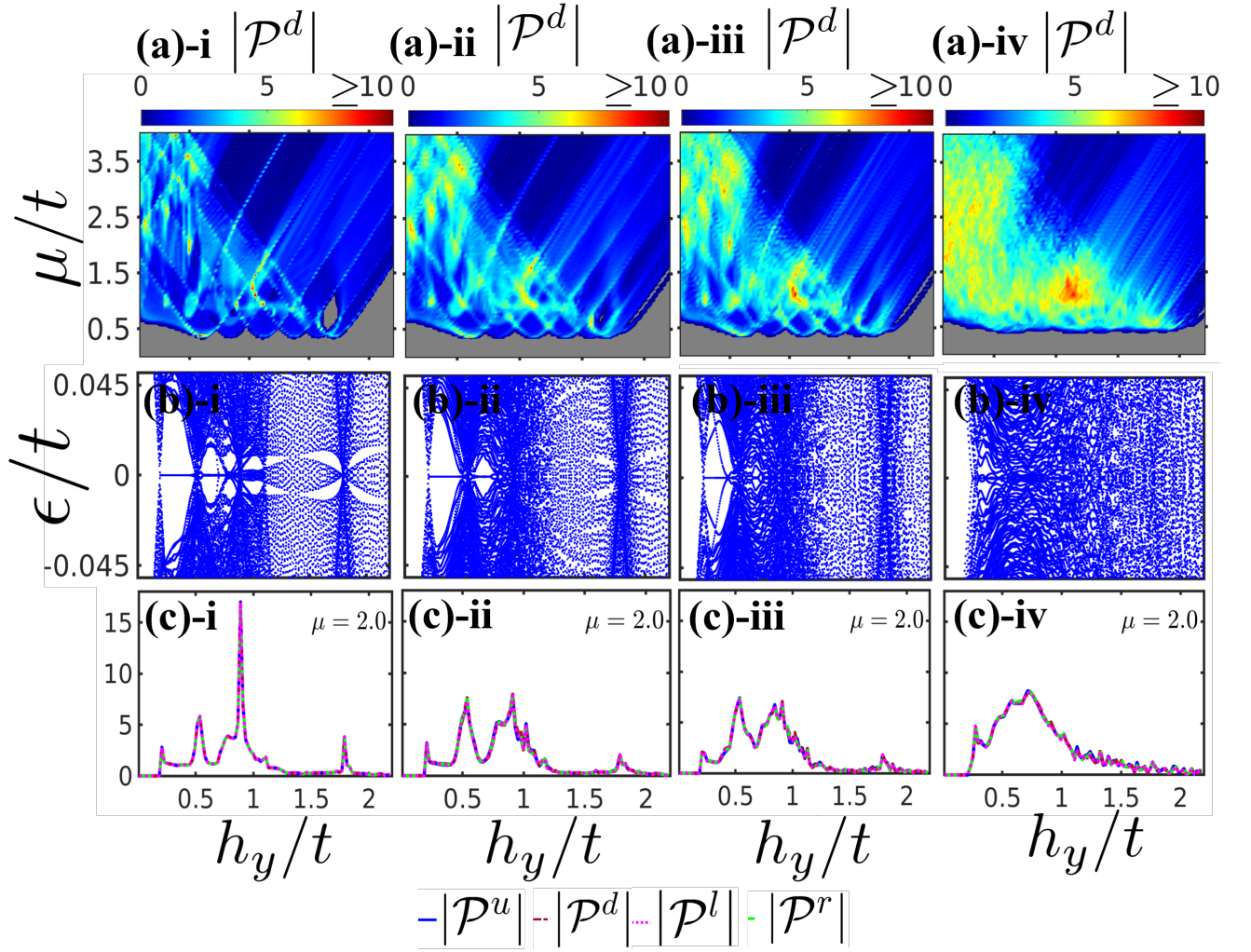


Figure 5. Majorana polarization in a finite-size **zigzag** graphene strip. Each column (i-iv) corresponds to a different disorder strength: (i) clean system (no disorder), (ii) weak disorder ( $\mathcal{Z} = 20$ ), 20 impurities,  $V_0 = 1.0$ , (iii) moderate disorder ( $\mathcal{Z} = 50$ ), 50 impurities,  $V_0 = 1.0$ , (iv) strong disorder ( $\mathcal{Z} = 150$ ), 150 impurities,  $V_0 = 1.5$ . Panels: (a) Heatmap of the absolute value of Majorana polarization in the lower half of the strip,  $|\mathcal{P}^d|$ , as a function of Zeeman energy ( $h_y/t$ ) and chemical potential ( $\mu/t$ ). (b) Energy spectrum as a function of  $h_y/t$  at fixed chemical potential  $\mu = 2.0$ . (c) Absolute value of Majorana polarization  $|\mathcal{P}^\nu|$  with  $\nu = u, d, l, r$  (upper, lower, left, right halves) as a function of  $h_y/t$ , also at  $\mu = 2.0$ .

(armchair) case, where a few broad, overlapping triangular features dominate. These features are attributed to the different boundary conditions and sublattice terminations along the zigzag edge, which affect the localization and interference patterns of quasiparticle modes. As disorder increases, these sharp features become increasingly diffused and less well-defined. The second row [panels (b)-i to (b)-iv] shows the low-energy spectra at  $\mu/t = 2.0$ . In contrast to the A-type system, where zero-energy modes persist over broader  $h_x/t$  intervals, the Z-type strip features several narrow, discrete regions in  $h_y/t$  where zero-energy states appear. These localized topological phases become increasingly unstable under disorder: as the disorder strength grows, the energy gaps close and non-topological low-energy states fill in, effectively destroying many of these narrow zero-energy win-

dows. The third row [panels (c)-i to (c)-iv] presents the Majorana polarization as a function of  $h_y/t$  for a fixed chemical potential  $\mu/t = 2.0$ , with polarization contributions plotted for four spatial regions of the strip. We note that in disordered systems as well, MP can be nonzero due to partially separated Andreev-bound states, which are not topologically protected.

To further investigate the existence and spatial character of Majorana modes in the Z-type strip, we analyze the zero-energy wavefunctions corresponding to selected values of the Zeeman field  $h_y/t$ . From the low-energy spectra presented earlier [Fig. 5(b)], we identify two parameter regions—approximately  $h_y/t \in [0.22, 0.45]$  and  $h_y/t \in [0.60, 0.70]$ —where zero-energy states persist and the spectrum remains gapped even in the presence of weak and moderate disorder. To probe the nature of the



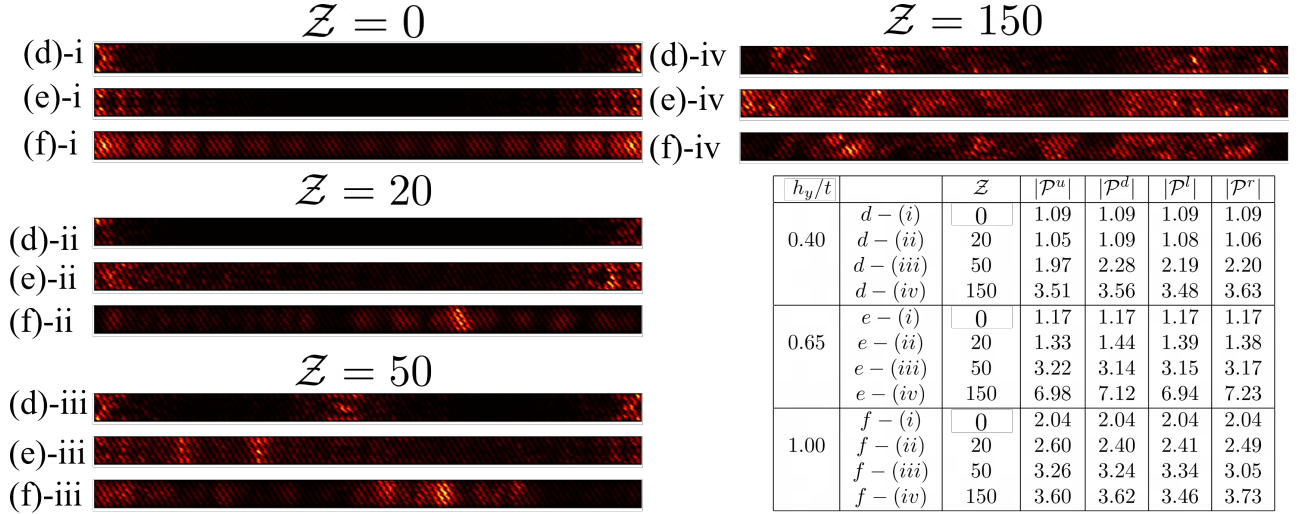


Figure 6. Real-space probability distribution of the low-energy Majorana modes on a **zigzag** graphene nanoribbon under varying magnetic field and disorder strength. Panels (d)-(e) correspond to increasing values of Zeeman field  $h_y/t = 0.40, 0.65$ , and  $1.00$ , respectively, at fixed chemical potential  $\mu/t = 2.0$ . Each row (i-iv) shows the effect of increasing disorder strength: (i) Clean (no disorder), (ii) Weak disorder ( $Z = 20$ ,  $V_0 = 1.0$ ), (iii) Moderate disorder ( $Z = 50$ ,  $V_0 = 1.0$ ), and (iv) Strong disorder ( $Z = 150$ ,  $V_0 = 1.5$ ). The adjacent table presents the absolute value of the Majorana polarization  $|P|$  for the lower ( $P^d$ ), upper ( $P^u$ ), left ( $P^l$ ), and right ( $P^r$ ) halves of the strip for each case.

zero-energy modes in these regions, we present wavefunction plots in Fig. 6 for  $h_y/t = 0.40, 0.65$ , and  $1.00$ , each representative of a distinct phase. Panels (d)-i and (e)-i of Fig. 6 (clean system) show that for  $h_y/t = 0.40$  and  $0.65$ , the zero-energy modes are localized at the shorter (armchair) edges of the strip. It is important to note that edge localization in Z-type strips (shorter edges are armchair) is qualitatively different from that in A-type strips (shorter edges are zigzag). In the A-type system, the wavefunctions tend to exhibit sharp, confined peaks at the zigzag boundaries, whereas in the Z-type case, the intensity is more distributed along the edge, with a broader spatial profile. Panel (f)-i shows a similar edge-localized structure for  $h_y/t = 1.00$ , although with wavefunction intensity gradually decreasing from both ends toward the center. In the presence of weak disorder ( $Z = 20$ ), the edge-localized features for  $h_y/t = 0.40$  and  $0.65$  persist [panels (d)-ii, (e)-ii], indicating robustness of the corresponding topological modes. At moderate disorder ( $Z = 50$ ), however, we begin to observe the emergence of additional localized features in the bulk of the strip [panels (d)-iii, (e)-iii], suggesting the coexistence of trivial modes. Under strong disorder ( $Z = 150$ ), the wavefunctions become fully delocalized or randomly localized, indicating that topological protection has been lost [panels (d)-iv, (e)-iv]. For  $h_y/t = 1.00$ , although the energy spectrum remains gapped, a high density of near zero-energy states appears even in the clean limit. This is reflected in the wavefunction plots (f)-ii and (f)-iii, where the edge-localized features become less distinct and partially separated Andreev bound states (ps-ABS) emerge. These states mimic Majorana signatures but

lack the topological protection required for true Majorana zero modes.

### C. Square

After analyzing armchair (A-type) and zigzag (Z-type) graphene strips, we now turn to a system with nearly square geometry. We refer to it as “nearly square” due to anisotropies in the graphene lattice that prevent the geometry from being perfectly symmetric in both directions (see Fig. 1 (c)). Along the vertical ( $y$ ) direction, the distance between two adjacent A-sublattice sites lying on the same column is  $\sqrt{3}a$ , while along the horizontal ( $x$ ) direction, the corresponding distance between A-sublattice sites on the same row is  $3a$ , where  $a$  denotes the lattice constant. Thus, to approximate a square geometry while maintaining consistent spatial coverage and a comparable number of lattice sites to the armchair and zigzag systems, we choose  $N = 35$  and  $L = 15$ . This configuration yields a geometry that is not strictly square but sufficiently close to allow a meaningful comparison of topological properties across different edge orientations, without introducing a significant bias due to system size.

If we apply an in-plane magnetic field, we find no clear phase separation or gapped regions so we primarily discuss the perpendicular magnetic field configuration, i.e., we apply the Zeeman field along the  $z$ -direction. The first row [panels (a)-i to (a)-iv] of Fig. 7 displays the phase diagrams for the nearly square geometry under increasing disorder. The clean system [panel (a)-i] reveals a characteristic pattern of overlapping triangular regions

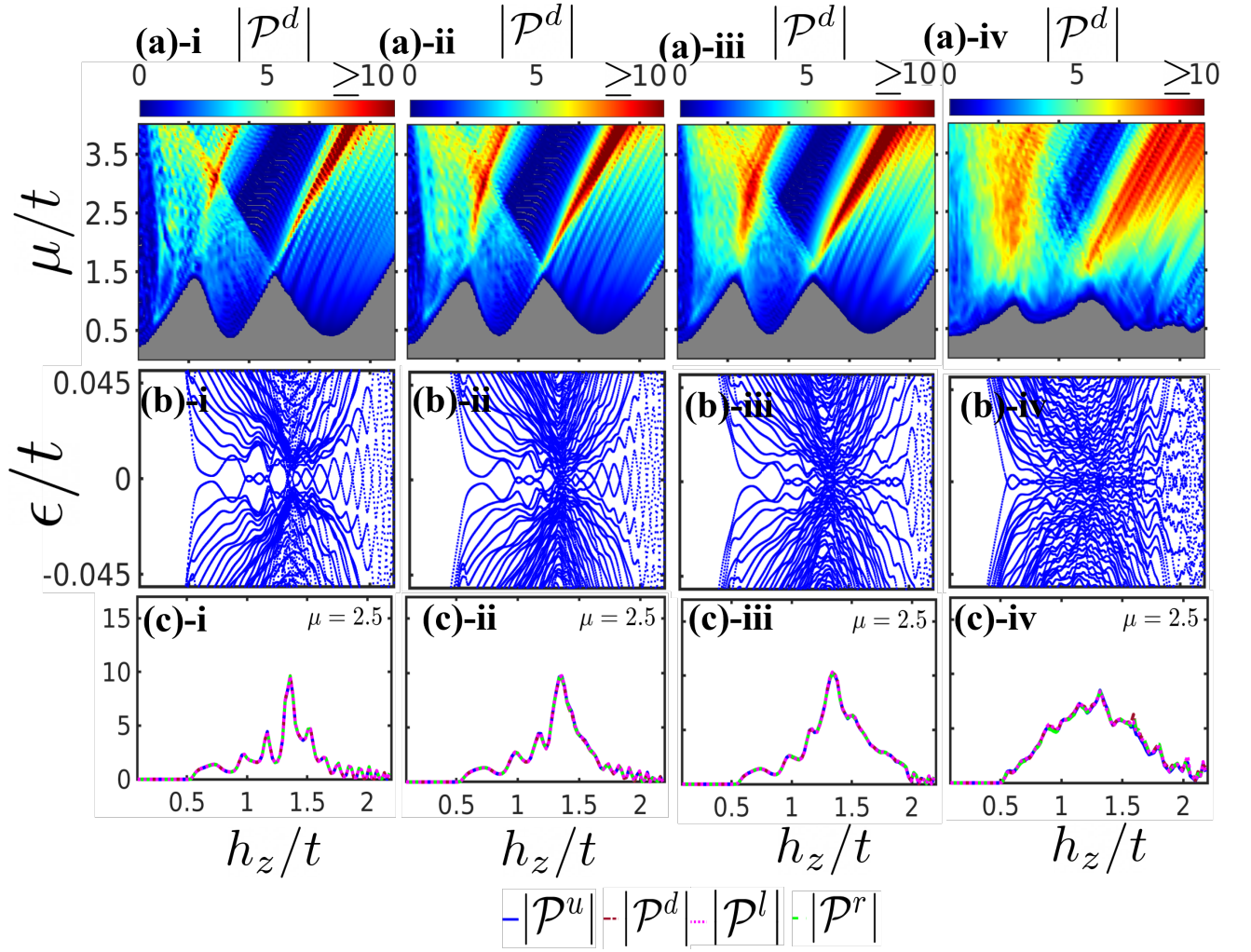


Figure 7. Majorana polarization in a finite-size **nearly square** shaped graphene geometry with **out-of-plane** magnetic field. Each column (i-iv) corresponds to a different disorder strength: (i) clean system (no disorder), (ii) weak disorder ( $\mathcal{Z} = 20$ ), 20 impurities,  $V_0 = 1.0$ , (iii) moderate disorder ( $\mathcal{Z} = 50$ ), 50 impurities,  $V_0 = 1.0$ , (iv) strong disorder ( $\mathcal{Z} = 150$ ), 150 impurities,  $V_0 = 1.5$ . Panels: (a) Heatmap of the absolute value of Majorana polarization in the lower half of the strip,  $|\mathcal{P}^d|$ , as a function of Zeeman energy ( $h_z/t$ ) and chemical potential ( $\mu/t$ ). (b) Energy spectrum as a function of  $h_z/t$  at fixed chemical potential  $\mu = 2.5$ . (c) Absolute value of Majorana polarization  $|\mathcal{P}^\nu|$  with  $\nu = u, d, l, r$  (upper, lower, left, right halves) as a function of  $h_z/t$ , also at  $\mu = 2.5$ .

in the  $(\mu/t, h_z/t)$  parameter space, similar in structure to those seen in armchair and zigzag strips. Figures 7(a)-i,iv and 3(a)-i,iv (or 5 (a)-i,iv) compare the  $(\mu/t, h_z/t)$  phase diagrams for square and armchair (or zigzag) geometry, we can observe that for the square geometry, the largest distortion in the topological phase occur predominantly in the upper-right quadrant of the parameter space, corresponding to high chemical potential and high magnetic field. In contrast, for the armchair geometry, the topological phase is mainly concentrated in the low-field regime (upper-left and lower-left quadrants), with only faint signatures in the high-field region, as the disorder strength increases. The second row [panels (b)-i to (b)-iv] presents the low-energy spectra, as a function of  $h_z/t$  at fixed  $\mu = 2.5$ . In the clean limit [panel

(b)-i], we observe gap closings and reopenings, pointing towards topological phase transitions. However, unlike the armchair and zigzag cases, where extended regions of zero-energy states were observed, the square geometry exhibits more discrete, oscillatory zero-energy modes. As disorder increases, the low-energy states begin to accumulate near zero energy, but lack a clear separation from the bulk spectrum. Under strong disorder, [panel (b)-iv], clear gap openings and reopenings are absent. To further probe the nature of the low-energy states observed in Fig. 7, we examine the spatial distribution of their corresponding wavefunctions in Fig. 8. These plots represent selected eigenstates at zero energy for three representative values of the Zeeman field:  $h_z/t = 0.70$ , 1.00, and 1.75, chosen from regions that exhibit mod-

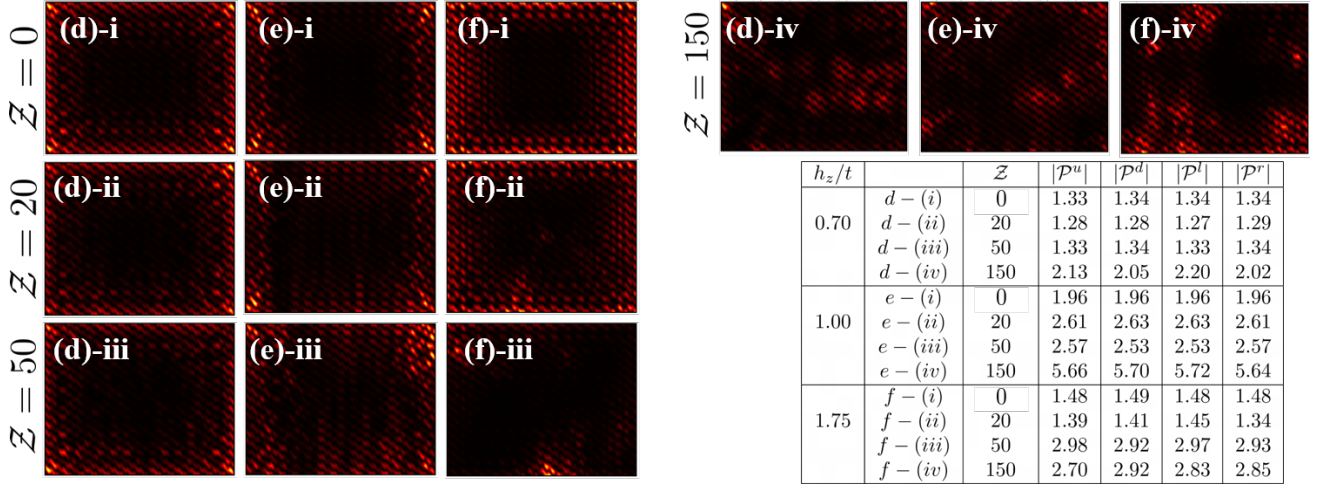


Figure 8. Real-space probability distribution of the low-energy Majorana modes on a nearly **square** graphene geometry under varying **out-of-plane** magnetic field and disorder strength. Panels (d)-(f) correspond to increasing values of Zeeman field  $h_z/t = 0.70, 1.00$ , and  $1.75$ , respectively, at fixed chemical potential  $\mu/t = 2.5$ . Each row (i-iv) shows the effect of increasing disorder strength: (i) Clean (no disorder), (ii) Weak disorder ( $Z = 20$ ,  $V_0 = 1.0$ ), (iii) Moderate disorder ( $Z = 50$ ,  $V_0 = 1.0$ ), and (iv) Strong disorder ( $Z = 150$ ,  $V_0 = 1.5$ ). The adjacent table presents the absolute value of the Majorana polarization  $|\mathcal{P}|$  for the lower ( $\mathcal{P}^d$ ), upper ( $\mathcal{P}^u$ ), left ( $\mathcal{P}^l$ ), and right ( $\mathcal{P}^r$ ) halves of the strip for each case.

erate to high polarization and indications of topological signatures. Each row corresponds to increasing disorder strength: clean ( $Z = 0$ ),  $Z = 20$ ,  $Z = 50$ , and  $Z = 150$ , respectively. In the clean system [panels (d)-i to (f)-i], the wavefunctions for  $h_z/t = 0.70$  and  $1.00$  show localization along the system boundaries, particularly at the corners and edges. This boundary-localized intensity, suggests the emergence of Majorana bound states (MBS) confined near the system's periphery. At  $h_z/t = 1.75$  [panel (f)-i], although some edge intensity persists, the mode appears more spread and less sharply confined, indicating that this regime may correspond to a partially separated Andreev bound state (ps-ABS) rather than a topologically protected MBS. As disorder is introduced [panels (d-f)-ii and (d-f)-iii], the wavefunctions maintain edge-localized features at  $h_z/t = 1.00$ , confirming that the second topological phase observed in the phase diagrams is robust up to moderate disorder. However, for  $h_z/t = 0.70$  and  $1.75$ , the localization becomes increasingly fragmented, and the amplitude shifts toward interior regions of the strip, indicating that disorder weakens or destroys the topological character of these states more rapidly outside the  $h_z/t \approx 1.00$  regime. In the strongly disordered case [panels (d-f)-iv], all wavefunctions lose clear spatial structure and exhibit random localization throughout the bulk. No clear edge confinement is visible, consistent with the mixing of low-energy states seen in the spectrum and the breakdown of the gapped regions in the phase diagrams. This confirms that the topological character of the system is lost under strong disorder, and the surviving zero-energy modes are trivial in nature.

#### D. Additional Cases

For completeness, we have also studied the A-type strip under a magnetic field applied along the  $y$ - and the  $Z$ -type strip under the field along the  $x$ -direction (i.e., field along the shorter directions). We also study both of them under a magnetic field in the  $z$ -direction as well. For the A-type geometry, we find that an in-plane field along the  $y$ -direction fails to produce any significant topological features: the phase diagrams remain distorted, and the low-energy spectra are dominated by states merged with the bulk, with no clear gapped regions. A similar lack of non-trivial behavior is observed in the  $Z$ -type strip when the magnetic field is applied in the  $x$ -direction. In both cases, the phase plots show no well-defined topological structure, and no isolated zero-energy modes are found. In contrast, the application of an out-of-plane ( $z$ -direction) magnetic field yields interesting topological behavior in both geometries. Since the essential qualitative features have already been discussed in earlier sections, the corresponding figures and discussions are relegated to the Appendix.

## VI. CONCLUSIONS AND OUTLOOK

Although graphene-based platforms for realizing Majorana modes have been examined in some earlier works, a unified understanding that connects geometry, magnetic orientation, disorder, and Andreev-state correlations has been missing. We revisited Majorana zero modes in proximitized graphene strips and examined under what conditions the observed zero-energy states correspond to gen-



uinely nonlocal Majoranas rather than partially separated Andreev bound states (quasi-Majoranas). Building on earlier works that introduced Majorana polarization as a spatial diagnostic [68, 69], we developed a systematic framework specific to graphene. Using a minimal tight-binding model that includes proximity-induced superconductivity, Zeeman coupling with tunable orientation, and site-dependent potential fluctuations (disorder), we correlated spectral evolution, MP distribution, and real-space wave-function morphology to identify regimes supporting robust, non-overlapping edge modes. Specifically, we studied finite strips with armchair (A-type), zigzag (Z-type), and square (S) geometry, allowing us to track how different terminations modify the low-energy spectrum and spatial character of the bound states. By systematically analyzing all three geometries under magnetic fields oriented along the  $x$ -,  $y$ -, and  $z$ -axes, we find that both edge termination and field orientation critically determine the presence and robustness of Majorana modes. Among these, the A-type strips, with shorter zigzag edges, emerge as the most favorable hosts, exhibiting well-defined, gapped zero-energy phases with sharply localized edge states and finite Majorana polarization, even under moderate to strong disorder. In these systems, both in-plane ( $x$ ) and out-of-plane ( $z$ ) magnetic fields yield robust topological features. For Z-type strips, with shorter armchair edges, topological phases also emerge for both in-plane ( $y$ ) and out-of-plane ( $z$ ) magnetic fields. Here, zero-energy modes appear within comparable parameter ranges but exhibit slightly broader spatial profiles near the edges than in A-type strips, where localization is sharper. In Fig. 1(a), which corresponds to an A-type strip with zigzag-terminated short edges, the two ends are sublattice polarized: the red and black dots denote the A and B sublattices, respectively, so the left boundary contains only A-sublattice sites, whereas the right boundary contains only B-sublattice sites. Such one-sublattice termination is characteristic of zigzag edges and gives rise to sublattice-polarized zero-energy states, in which the wavefunction has finite amplitude only on the terminating sublattice while the opposite component is forced to vanish by the tight-binding boundary conditions [84]. In contrast, armchair edges include both A and B sublat-

tices at the boundary; the corresponding boundary condition mixes the two components rather than suppressing either of them. As a result, armchair edges do not support sublattice-polarized zero modes, and their low-energy states extend across the nanoribbon. These distinctions underlie the much sharper localization of Majorana bound states at zigzag edges compared to armchair edges in proximitized graphene nanoribbons. In the S-type geometry, topological phases occur only when the magnetic field is applied along the  $z$ -direction. The corresponding wavefunctions display corner modes and edge localization along all four sides, with moderate spatial spread. These corner and edge states remain robust against weak to moderate disorder.

Looking forward, several open directions emerge. Computing a bulk or scattering topological invariant for finite graphene strips would establish an unambiguous correspondence between MP-based diagnostics and the underlying topological class. Investigating how the ground-state splitting scales with system length would further clarify the nonlocal nature of the modes. Incorporating self-consistent electrostatics and spatially varying pairing potentials could improve quantitative accuracy, while multiterminal configurations may reveal nonlocal conductance signatures unique to Majorana pairs. Our results elevate graphene from a conceptual setting to a controllable material platform where the interplay of geometry, magnetic orientation, and potential landscape can be exploited to engineer, stabilize, and unambiguously identify Majorana-bound states. In addition, recent progress on the periodic disorder invariant (PDI), which constructs a bulk topological invariant by periodically repeating a finite disordered segment [85], offers a promising future route for diagnosing disorder-robust Majorana zero modes and distinguishing them from trivial zero-energy states in proximitized graphene nanoribbons.

*Acknowledgment:* G.S. was funded by ANRF-SERB Core Research Grant CRG/2023/005628. S.K. was funded by IIT Mandi HTRA fellowship. S.T. acknowledges ARO Grant W911NF2210247. We thank Ekta for independently verifying our results using a KWANT-based numerical implementation.

## Appendix A: Armchair with out-of-plane Zeeman field

We analyze the spectral and polarization plots for the armchair strip in the presence of disorder with an out-of-plane magnetic field, as shown in Fig. 9. The low-energy spectra in panels (b)–i–iv reveal two distinct topological regions, where zero-energy modes persist when the magnetic field lies in the ranges  $h_z/t \approx 0.4$ – $1.2$  and  $1.5$ – $1.9$ , with the chemical potential fixed at  $\mu/t = 2.5$ . Importantly, the bulk gap remains open up to moderate disorder, indicating robustness of the topological phase. Complementary evidence for topological regions comes from the polarization plots in panels (c)–i–iv, which display two sharp peaks characteristic of topological phase transitions. Within the above field ranges, the polarization remains stable in the clean system and exhibits only small oscillations as the disorder strength increases. Further insight is obtained from the wavefunction profiles in Fig. 10. Robust Majorana zero modes are clearly observed in panels (f)–i–iii, corresponding to clean to moderately disordered systems at  $h_z/t = 1.70$ .



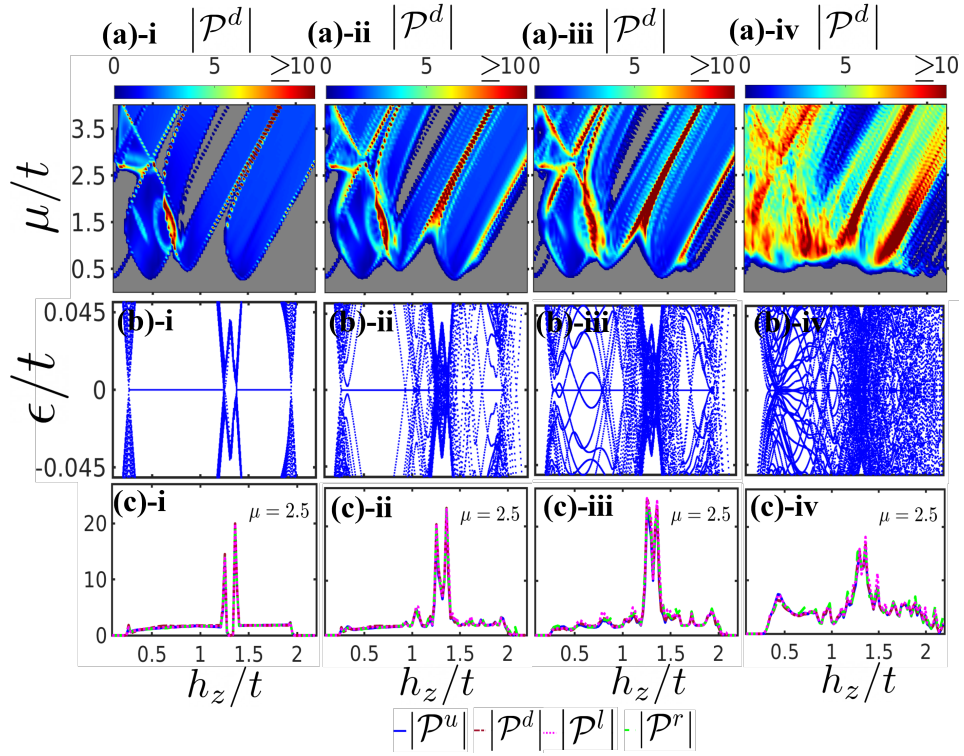


Figure 9. Majorana polarization in a finite-size **armchair** graphene strip for **out-of-plane magnetic field**. Each column (i-iv) corresponds to a different disorder strength: (i) clean system (no disorder), (ii) weak disorder ( $\mathcal{Z} = 20$ ), 20 impurities,  $V_0 = 1.0$ , (iii) moderate disorder ( $\mathcal{Z} = 50$ ), 50 impurities,  $V_0 = 1.0$ , (iv) strong disorder ( $\mathcal{Z} = 150$ ), 150 impurities,  $V_0 = 1.5$ . Panels: (a) Heatmap of the absolute value of Majorana polarization in the lower half of the strip,  $|\mathcal{P}^d|$ , as a function of Zeeman energy ( $h_z/t$ ) and chemical potential ( $\mu/t$ ). (b) Energy spectrum as a function of  $h_z/t$  at fixed chemical potential  $\mu = 2.5$ . (c) Absolute value of Majorana polarization  $|\mathcal{P}^\nu|$  with  $\nu = u, d, l, r$  (upper, lower, left, right halves) as a function of  $h_z/t$ , also at  $\mu = 2.5$ .

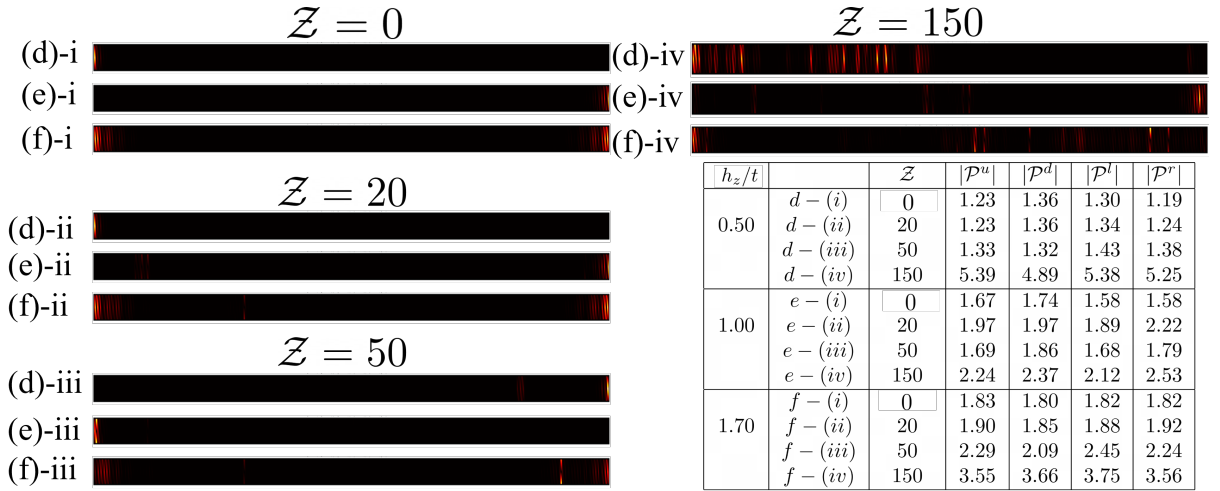


Figure 10. Real-space probability distribution of the low-energy Majorana modes on an **armchair** graphene nanoribbon under varying **out-of-plane magnetic field** and disorder strength. Panels (d)-(f) correspond to increasing values of Zeeman field  $h_z/t = 0.50, 1.00$ , and  $1.70$ , respectively, at fixed chemical potential  $\mu/t = 2.5$ . Each row (i-iv) shows the effect of increasing disorder strength: (i) Clean (no disorder), (ii) Weak disorder ( $\mathcal{Z} = 20$ ,  $V_0 = 1.0$ ), (iii) Moderate disorder ( $\mathcal{Z} = 50$ ,  $V_0 = 1.0$ ), and (iv) Strong disorder ( $\mathcal{Z} = 150$ ,  $V_0 = 1.5$ ). The adjacent table presents the absolute value of the Majorana polarization  $|\mathcal{P}|$  for the lower ( $\mathcal{P}^d$ ), upper ( $\mathcal{P}^u$ ), left ( $\mathcal{P}^l$ ), and right ( $\mathcal{P}^r$ ) halves of the strip for each case.

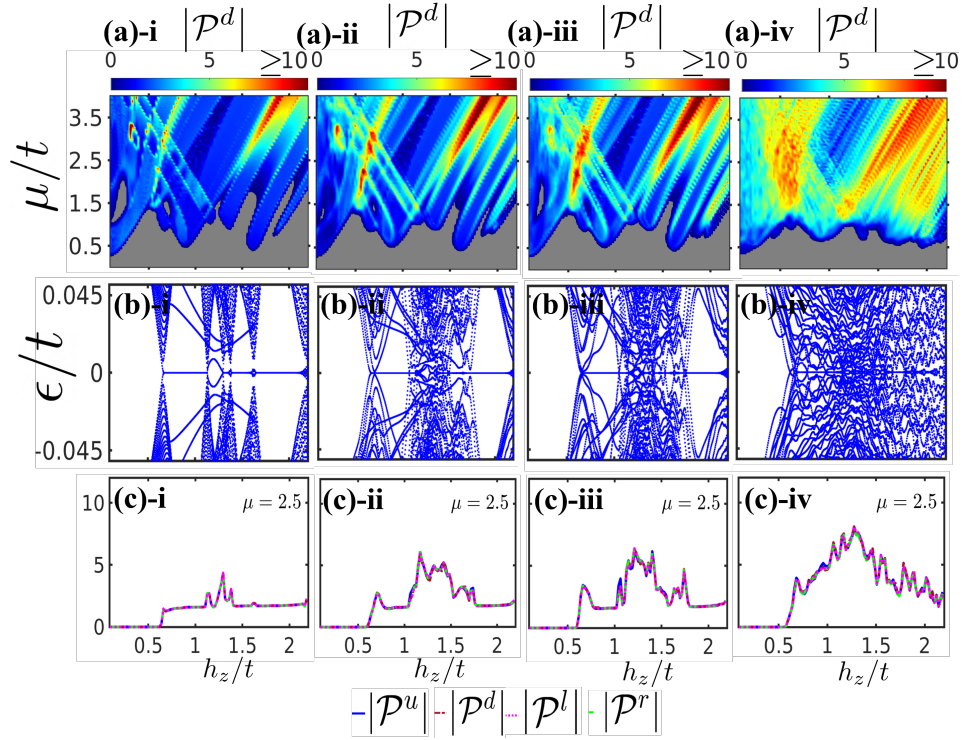


Figure 11. Majorana polarization in a finite-size **zigzag** graphene strip for **out-of-plane magnetic field**. Each column (i-iv) corresponds to a different disorder strength: (i) clean system (no disorder), (ii) weak disorder ( $\mathcal{Z} = 20$ ), 20 impurities,  $V_0 = 1.0$ , (iii) moderate disorder ( $\mathcal{Z} = 50$ ), 50 impurities,  $V_0 = 1.0$ , (iv) strong disorder ( $\mathcal{Z} = 150$ ), 150 impurities,  $V_0 = 1.5$ . Panels: (a) Heatmap of the absolute value of Majorana polarization in the lower half of the strip,  $|\mathcal{P}^d|$ , as a function of Zeeman energy ( $h_z/t$ ) and chemical potential ( $\mu/t$ ). (b) Energy spectrum as a function of  $h_z/t$  at fixed chemical potential  $\mu = 2.5$ . (c) Absolute value of Majorana polarization  $|\mathcal{P}^\nu|$  with  $\nu = u, d, l, r$  (upper, lower, left, right halves) as a function of  $h_z/t$ , also at  $\mu = 2.5$ .

These Majorana modes are sharply localized at the strip ends. In contrast, panel (d)-iv reveals partially separated Andreev bound states, while panels (e)-i-iii display states localized at a single edge with finite polarization, signifying trivial modes. The phase diagram for the A-type geometry primarily exhibits a triangular pattern, which gradually distorts with increasing disorder at higher  $\mu/t$  and  $h_z/t$  values. The low-energy spectrum reveals multiple gapped regions supporting zero-energy modes, whose corresponding wavefunctions remain sharply localized at the zigzag (shorter) edges. This localization persists even under moderate to strong disorder, signaling the emergence of robust, topologically protected Majorana bound states (MBS). Occasionally, however, we find wavefunctions localized at a single edge, consistent with partially separated Andreev bound states (ps-ABS), which are topologically trivial.

## Appendix B: ZigZag with out-of-plane Zeeman field

We now turn to the zigzag strip in the presence of disorder and an out-of-plane magnetic field, as shown in Fig. 11. The low-energy spectra in panels (b)-i-iii, obtained at fixed chemical potential  $\mu/t = 2.5$ , exhibit three regions with zero-energy states. Among these, two field ranges,  $h_z/t \approx 0.6-1.1$  and  $1.4-2.1$ , retain both an open bulk gap and robust zero-energy modes up to moderate disorder, suggesting the stability of Majorana zero modes. The corresponding polarization plots in panels (c)-i-iii confirm this picture: the Majorana polarization remains nearly stable across these field ranges, even as the disorder strength increases. Further insight is obtained from the wavefunction profiles shown in Fig. 12. In contrast to the armchair strip, where the modes are sharply localized at the ends, the Majorana modes in the zigzag geometry are more spatially extended near the edges. Panels (d)-i-iii reveal robust Majorana zero modes persisting up to moderate disorder at both ends of the strip, while panels (e)-ii-iii display modes with partial localization at the center of the strip. At strong disorder, however, the zero-energy states lose their topological protection and evolve into partially separated Andreev bound states, as illustrated in panels (d,e,f)-iv. The phase diagram for the Z-type geometry shows a similar triangular pattern, which becomes increasingly distorted with disorder. Here too, gapped regions host zero-energy states under an out-of-plane magnetic

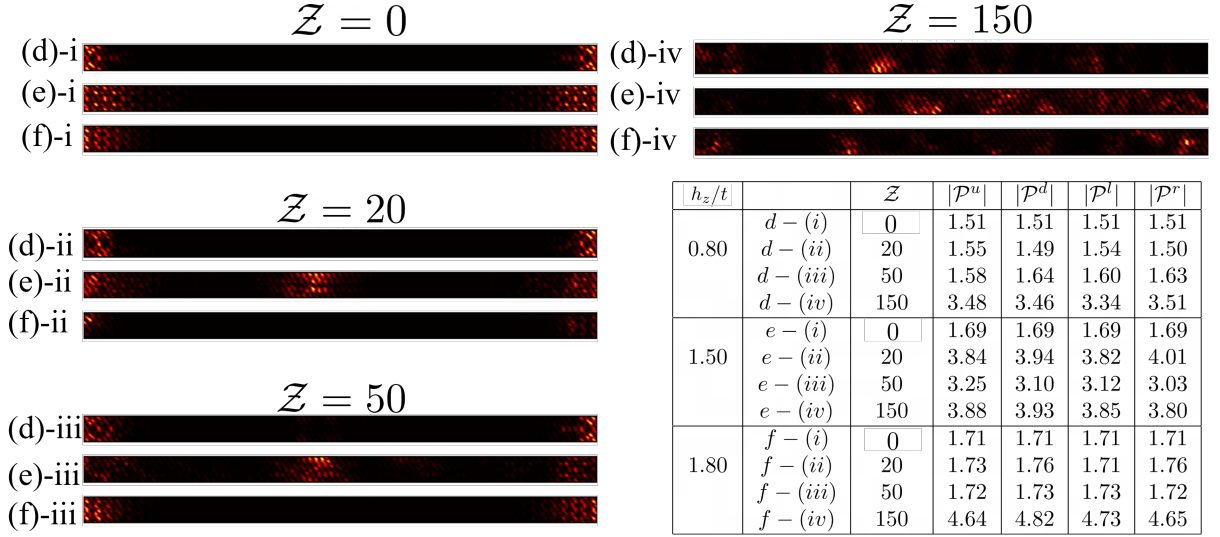


Figure 12. Real-space probability distribution of the low-energy Majorana modes on a **zigzag** graphene nanoribbon under varying **out-of-plane magnetic field** and disorder strength. Panels (d)-(f) correspond to increasing values of Zeeman field  $h_z/t = 0.80, 1.50$ , and  $1.80$ , respectively, at fixed chemical potential  $\mu/t = 2.5$ . Each row (i-iv) shows the effect of increasing disorder strength: (i) Clean (no disorder), (ii) Weak disorder ( $\mathcal{Z} = 20$ ,  $V_0 = 1.0$ ), (iii) Moderate disorder ( $\mathcal{Z} = 50$ ,  $V_0 = 1.0$ ), and (iv) Strong disorder ( $\mathcal{Z} = 150$ ,  $V_0 = 1.5$ ). The adjacent table presents the absolute value of the Majorana polarization  $|\mathcal{P}|$  for the lower ( $\mathcal{P}^d$ ), upper ( $\mathcal{P}^u$ ), left ( $\mathcal{P}^l$ ), and right ( $\mathcal{P}^r$ ) halves of the strip for each case.

field. However, a clear distinction arises between the in-plane ( $y$ -direction) and out-of-plane ( $z$ -direction) field cases: while in-plane fields produce multiple narrow topological transitions that are fragile under disorder, the  $z$ -field results in broader topological regions, comparable to those in the A-type strip. The associated wavefunctions are less sharply localized, spreading over the edge regions, indicating that although MBS-like states may exist, their localization is weaker compared to the A-type geometry.

Comparing the two edge terminations, we find that while both armchair and zigzag strips support robust Majorana modes over finite ranges of magnetic field and disorder, their spatial character differs substantially. In the armchair case, the modes are sharply localized at the strip ends, whereas in the zigzag case the modes tend to spread along the edges or partially extend into the bulk. This qualitative distinction highlights the role of edge geometry in shaping the robustness and localization properties of Majorana zero modes in graphene nanoribbons.

- 
- [1] E. Majorana, *Nuovo Cimento* **14**, 171 (1937).
  - [2] S. Das Sarma, In search of majorana, *Nature Physics* **19**, 165 (2023).
  - [3] G. Moore and N. Read, Nonabelions in the fractional quantum hall effect, *Nuclear Physics B* **360**, 362 (1991).
  - [4] N. Read and D. Green, Paired states of fermions in two dimensions with breaking of parity and time-reversal symmetries and the fractional quantum hall effect, *Physical Review B* **61**, 10267 (2000).
  - [5] C. Nayak and F. Wilczek, 2n-quasihole states realize 2n-1-dimensional spinor braiding statistics in paired quantum hall states, *Nuclear Physics B* **479**, 529 (1996).
  - [6] A. Y. Kitaev, *Annals. Phys.* **303**, 2 (2003).
  - [7] C. Nayak, S. H. Simon, A. Stern, M. Freedman, and S. Das Sarma, Non-abelian anyons and topological quantum computation, *Rev. Mod. Phys.* **80**, 1083 (2008).
  - [8] J. D. Sau, R. M. Lutchyn, S. Tewari, and S. D. Sarma, Generic new platform for topological quantum computation using semiconductor heterostructures, *Physical review letters* **104**, 040502 (2010).
  - [9] J. D. Sau, S. Tewari, R. M. Lutchyn, T. D. Stanescu, and S. D. Sarma, Non-abelian quantum order in spin-orbit-coupled semiconductors: Search for topological majorana particles in solid-state systems, *Physical Review B* **82**, 214509 (2010).
  - [10] Y. Oreg, G. Refael, and F. von Oppen, Helical liquids and majorana bound states in quantum wires, *Physical review letters* **105**, 177002 (2010).
  - [11] R. M. Lutchyn, J. D. Sau, and S. D. Sarma, Majorana fermions and a topological phase transition in semiconductor-superconductor heterostructures, *Physical review letters* **105**, 077001 (2010).
  - [12] K. Sengupta, I. Žutić, H.-J. Kwon, V. M. Yakovenko, and S. D. Sarma, Midgap edge states and pairing symmetry of quasi-one-dimensional organic superconductors, *Physical Review B* **63**, 144531 (2001).

- [13] K. Law, P. A. Lee, and T. Ng, Majorana fermion induced resonant andreev reflection, *Physical review letters* **103**, 237001 (2009).
- [14] K. Flensberg, Tunneling characteristics of a chain of majorana bound states, *Physical Review B* **82**, 180516 (2010).
- [15] V. Mourik, K. Zuo, S. M. Frolov, S. Plissard, E. P. Bakkers, and L. P. Kouwenhoven, Signatures of majorana fermions in hybrid superconductor-semiconductor nanowire devices, *Science* **336**, 1003 (2012).
- [16] M. Deng, C. Yu, G. Huang, M. Larsson, P. Caroff, and H. Xu, Anomalous zero-bias conductance peak in a nb-insb nanowire-nb hybrid device, *Nano letters* **12**, 6414 (2012).
- [17] A. Das, Y. Ronen, Y. Most, Y. Oreg, M. Heiblum, and H. Shtrikman, Zero-bias peaks and splitting in an al-inas nanowire topological superconductor as a signature of majorana fermions, *Nature Physics* **8**, 887 (2012).
- [18] L. P. Rokhinson, X. Liu, and J. K. Furdyna, The fractional ac josephson effect in a semiconductor-superconductor nanowire as a signature of majorana particles, *Nature Physics* **8**, 795 (2012).
- [19] H. Churchill, V. Fatemi, K. Grove-Rasmussen, M. Deng, P. Caroff, H. Xu, and C. M. Marcus, Superconductor-nanowire devices from tunneling to the multichannel regime: Zero-bias oscillations and magnetoconductance crossover, *Physical Review B* **87**, 241401 (2013).
- [20] A. Finck, D. J. Van Harlingen, P. Mohseni, K. Jung, and X. Li, Anomalous modulation of a zero-bias peak in a hybrid nanowire-superconductor device, *Physical review letters* **110**, 126406 (2013).
- [21] M. Deng, S. Vaitiekėnas, E. B. Hansen, J. Danon, M. Leijnse, K. Flensberg, J. Nygård, P. Krogstrup, and C. M. Marcus, Majorana bound state in a coupled quantum-dot hybrid-nanowire system, *Science* **354**, 1557 (2016).
- [22] H. Zhang, Ö. Gül, S. Conesa-Boj, M. P. Nowak, M. Wimmer, K. Zuo, V. Mourik, F. K. De Vries, J. Van Veen, M. W. De Moor, *et al.*, Ballistic superconductivity in semiconductor nanowires, *Nature communications* **8**, 16025 (2017).
- [23] J. Chen, P. Yu, J. Stenger, M. Hoeschele, D. Car, S. R. Plissard, E. P. Bakkers, T. D. Stanescu, and S. M. Frolov, Experimental phase diagram of zero-bias conductance peaks in superconductor/semiconductor nanowire devices, *Science advances* **3**, e1701476 (2017).
- [24] F. Nichele, A. C. Drachmann, A. M. Whiticar, E. C. O'Farrell, H. J. Suominen, A. Fornieri, T. Wang, G. C. Gardner, C. Thomas, A. T. Hatke, *et al.*, Scaling of majorana zero-bias conductance peaks, *Physical review letters* **119**, 136803 (2017).
- [25] S. Albrecht, E. Hansen, A. P. Higginbotham, F. Kuemmeth, T. Jespersen, J. Nygård, P. Krogstrup, J. Danon, K. Flensberg, and C. Marcus, Transport signatures of quasiparticle poisoning in a majorana island, *Physical review letters* **118**, 137701 (2017).
- [26] E. O. Farrell, A. Drachmann, M. Hell, A. Fornieri, A. Whiticar, E. Hansen, S. Gronin, G. Gardner, C. Thomas, M. Manfra, *et al.*, Hybridization of subgap states in one-dimensional superconductor-semiconductor coulomb islands, *Physical review letters* **121**, 256803 (2018).
- [27] J. Shen, S. Heedt, F. Borsoi, B. Van Heck, S. Gazibegovic, R. L. O. het Veld, D. Car, J. A. Logan, M. Pendharkar, S. J. Ramakers, *et al.*, Parity transitions in the superconducting ground state of hybrid insb-al coulomb islands, *Nature communications* **9**, 4801 (2018).
- [28] D. Sherman, J. Yodh, S. M. Albrecht, J. Nygård, P. Krogstrup, and C. M. Marcus, Normal, superconducting and topological regimes of hybrid double quantum dots, *Nature nanotechnology* **12**, 212 (2017).
- [29] S. Vaitiekėnas, A. Whiticar, M.-T. Deng, F. Krizek, J. Sestoft, C. Palmstrøm, S. Marti-Sanchez, J. Arbiol, P. Krogstrup, L. Casparis, *et al.*, Selective-area-grown semiconductor-superconductor hybrids: A basis for topological networks, *Physical review letters* **121**, 147701 (2018).
- [30] S. M. Albrecht, A. P. Higginbotham, M. Madsen, F. Kuemmeth, T. S. Jespersen, J. Nygård, P. Krogstrup, and C. Marcus, Exponential protection of zero modes in majorana islands, *Nature* **531**, 206 (2016).
- [31] P. Yu, J. Chen, M. Gomanko, G. Badawy, E. P. A. M. Bakkers, K. Zuo, V. Mourik, and S. M. Frolov, Non-majorana states yield nearly quantized conductance in proximitized nanowires, *Nature Physics* **17**, 482–488 (2021).
- [32] M. A. Quantum, M. Aghaee, A. Alcaraz Ramirez, Z. Alam, R. Ali, M. Andrzejczuk, A. Antipov, M. Astafev, A. Barzegar, B. Bauer, *et al.*, Interferometric single-shot parity measurement in inas-al hybrid devices, *Nature* **638**, 651 (2025).
- [33] D. Mondal, A. Pal, A. Saha, and T. Nag, Distinguishing between topological majorana and trivial zero modes via transport and shot noise study in an altermagnet heterostructure, *Physical Review B* **111**, L121401 (2025).
- [34] S. Głodzik, N. Sedlmayr, and T. Domański, How to measure the majorana polarization of a topological planar josephson junction, *Physical Review B* **102**, 085411 (2020).
- [35] L. Rossi, F. Dolcini, and F. Rossi, Majorana-like localized spin density without bound states in topologically trivial spin-orbit coupled nanowires, *Physical Review B* **101**, 195421 (2020).
- [36] Y. Tanaka, S. Tamura, and J. Cayao, Theory of majorana zero modes in unconventional superconductors, *Progress of Theoretical and Experimental Physics* **2024**, 08C105 (2024).
- [37] Y. Tanaka, M. Sato, and N. Nagaosa, Symmetry and topology in superconductors—odd-frequency pairing and edge states—, *Journal of the Physical Society of Japan* **81**, 011013 (2011).
- [38] G. Sharma and S. Tewari, Tunneling conductance for majorana fermions in spin-orbit coupled semiconductor-superconductor heterostructures using superconducting leads, *Physical Review B* **93**, 195161 (2016).
- [39] Y. Tanaka, T. Yokoyama, and N. Nagaosa, Manipulation of the majorana fermion, andreev reflection, and josephson current on topological insulators, *Physical review letters* **103**, 107002 (2009).
- [40] G. Kells, D. Meidan, and P. W. Brouwer, Near-zero-energy end states in topologically trivial spin-orbit coupled superconducting nanowires with a smooth confinement, *Phys. Rev. B* **86**, 100503 (2012).
- [41] S. Mi, D. I. Pikulin, M. Marciiani, and C. W. J. Beenakker, X-shaped and y-shaped andreev resonance profiles in a superconducting quantum dot, *Journal of Experimental and Theoretical Physics* **119**, 1018 (2014).
- [42] D. Bagrets and A. Altland, Class *d* spectral peak in



- majorana quantum wires, *Phys. Rev. Lett.* **109**, 227005 (2012).
- [43] D. I. Pikulin, J. Dahlhaus, M. Wimmer, H. Schomerus, and C. Beenakker, A zero-voltage conductance peak from weak antilocalization in a majorana nanowire, *New Journal of Physics* **14**, 125011 (2012).
- [44] E. Prada, P. San-Jose, and R. Aguado, Transport spectroscopy of *ns* nanowire junctions with majorana fermions, *Phys. Rev. B* **86**, 180503 (2012).
- [45] H. Pan and S. D. Sarma, Physical mechanisms for zero-bias conductance peaks in majorana nanowires, *Physical Review Research* **2**, 013377 (2020).
- [46] C. Moore, T. D. Stanescu, and S. Tewari, Two-terminal charge tunneling: Disentangling majorana zero modes from partially separated andreev bound states in semiconductor-superconductor heterostructures, *Physical Review B* **97**, 165302 (2018).
- [47] C. Moore, C. Zeng, T. D. Stanescu, and S. Tewari, Quantized zero-bias conductance plateau in semiconductor-superconductor heterostructures without topological majorana zero modes, *Physical Review B* **98**, 155314 (2018).
- [48] A. Vuik, B. Nijholt, A. R. Akhmerov, and M. Wimmer, Reproducing topological properties with quasi-majorana states, *arXiv preprint arXiv:1806.02801* (2018).
- [49] T. D. Stanescu and S. Tewari, Robust low-energy andreev bound states in semiconductor-superconductor structures: Importance of partial separation of component majorana bound states, *Phys. Rev. B* **100**, 155429 (2019).
- [50] P. San-Jose, J. Cayao, E. Prada, and R. Aguado, Majorana bound states from exceptional points in non-topological superconductors, *Scientific Reports* **6**, 21427 (2016).
- [51] J. Avila, F. Peñaranda, E. Prada, P. San-Jose, and R. Aguado, Non-hermitian topology as a unifying framework for the andreev versus majorana states controversy, *Communications Physics* **2**, 10.1038/s42005-019-0231-8 (2019).
- [52] O. A. Awoga, J. Cayao, and A. M. Black-Schaffer, Supercurrent detection of topologically trivial zero-energy states in nanowire junctions, *Phys. Rev. Lett.* **123**, 117001 (2019).
- [53] G. Sharma, C. Zeng, T. D. Stanescu, and S. Tewari, Hybridization energy oscillations of majorana and andreev bound states in semiconductor-superconductor nanowire heterostructures, *Physical Review B* **101**, 245405 (2020).
- [54] C. Zeng, G. Sharma, T. D. Stanescu, and S. Tewari, Feasibility of measurement-based braiding in the quasi-majorana regime of semiconductor-superconductor heterostructures, *Physical Review B* **102**, 205101 (2020).
- [55] C. Zeng, G. Sharma, S. Tewari, and T. Stanescu, Partially separated majorana modes in a disordered medium, *Physical Review B* **105**, 205122 (2022).
- [56] E. Prada, P. San-Jose, M. W. A. de Moor, A. Geresdi, E. J. H. Lee, J. Klinovaja, D. Loss, J. Nygård, R. Aguado, and L. P. Kouwenhoven, From andreev to majorana bound states in hybrid superconductor-semiconductor nanowires, *Nature Reviews Physics* 10.1038/s42254-020-0228-y (2020).
- [57] J. Cayao and A. M. Black-Schaffer, Distinguishing trivial and topological zero-energy states in long nanowire junctions, *Physical Review B* **104**, 10.1103/physrevb.104.1020501 (2021).
- [58] H. Zhang, M. W. A. de Moor, J. D. S. Bommer, D. Xu, G. Wang, N. van Loo, C.-X. Liu, S. Gazibegovic, J. A. Logan, D. Car, R. L. M. O. het Veld, P. J. van Veldhoven, S. Koelling, M. A. Verheijen, M. Pendharkar, D. J. Pennachio, B. Shojaei, J. S. Lee, C. J. Palmstrøm, E. P. A. M. Bakkers, S. D. Sarma, and L. P. Kouwenhoven, Large zero-bias peaks in insb-al hybrid semiconductor-superconductor nanowire devices (2021), [arXiv:2101.11456 \[cond-mat.mes-hall\]](#).
- [59] S. D. Sarma and H. Pan, Disorder-induced zero-bias peaks in majorana nanowires (2021), [arXiv:2103.05628 \[cond-mat.mes-hall\]](#).
- [60] S. Frolov, Quantum computing's reproducibility crisis: Majorana fermions, *Nature* **592**, 350 (2021).
- [61] R. Ma, M. Pizzochero, and G. Chaudhary, Graphene nanoribbons as a majorana platform, *arXiv preprint arXiv:2506.14999* (2025).
- [62] V. Kaladzhyan and C. Bena, Formation of majorana fermions in finite-size graphene strips, *SciPost Physics* **3**, 002 (2017).
- [63] V. Kaladzhyan, J. Despres, I. Mandal, and C. Bena, Majorana fermions in finite-size strips with in-plane magnetic fields, *The European Physical Journal B* **90**, 1 (2017).
- [64] P. San-Jose, J. L. Lado, R. Aguado, F. Guinea, and J. Fernández-Rossier, Majorana zero modes in graphene, *Phys. Rev. X* **5**, 041042 (2015).
- [65] K. Laubscher, D. Loss, and J. Klinovaja, Majorana and parafermion corner states from two coupled sheets of bilayer graphene, *Physical Review Research* **2**, 013330 (2020).
- [66] Z.-H. Wang, E. V. Castro, and H.-Q. Lin, Strain manipulation of majorana fermions in graphene armchair nanoribbons, *Physical Review B* **97**, 041414 (2018).
- [67] A. L. Manesco, G. Weber, and D. Rodrigues Jr, Effective model for majorana modes in graphene, *Physical Review B* **100**, 125411 (2019).
- [68] D. Sticlet, C. Bena, and P. Simon, Spin and majorana polarization in topological superconducting wires, *Physical Review Letters* **108**, 096802 (2012).
- [69] N. Sedlmayr and C. Bena, Visualizing majorana bound states in one and two dimensions using the generalized majorana polarization, *Physical Review B* **92**, 115115 (2015).
- [70] N. Sedlmayr, J. Aguiar-Hualde, and C. Bena, Majorana bound states in open quasi-one-dimensional and two-dimensional systems with transverse rashba coupling, *Physical Review B* **93**, 155425 (2016).
- [71] S. Karoliya, S. Tewari, and G. Sharma, Majorana polarization in disordered quasi-one-dimensional hybrid nanowires, *Physical Review B* **112**, 165410 (2025).
- [72] S. Tewari and J. D. Sau, Topological invariants for spin-orbit coupled superconductor nanowires, *Physical review letters* **109**, 150408 (2012).
- [73] O. A. Awoga and J. Cayao, Identifying trivial and majorana zero-energy modes using the majorana polarization, *Physical Review B* **110**, 165404 (2024).
- [74] H. B. Nielsen and M. Ninomiya, Absence of neutrinos on a lattice: (i). proof by homotopy theory, *Nuclear Physics B* **185**, 20 (1981).
- [75] H. B. Nielsen and M. Ninomiya, Absence of neutrinos on a lattice: (ii). intuitive topological proof, *Nuclear Physics B* **193**, 173 (1981).
- [76] H. B. Nielsen and M. Ninomiya, A no-go theorem for regularizing chiral fermions, *Physics Letters B* **105**, 219

- (1981).
- [77] C. W. J. Beenakker, A. Donís Vela, G. Lemut, M. J. Pacholski, and J. Tworzydło, Tangent fermions: Dirac or majorana fermions on a lattice without fermion doubling, *Annalen der Physik* **535**, 2300081 (2023).
  - [78] L. Brey and H. Fertig, Electronic states of graphene nanoribbons studied with the dirac equation, *Physical Review B—Condensed Matter and Materials Physics* **73**, 235411 (2006).
  - [79] B. A. Bernevig, Topological insulators and topological superconductors, in *Topological Insulators and Topological Superconductors* (Princeton university press, 2013).
  - [80] Y.-W. Son, M. L. Cohen, and S. G. Louie, Half-metallic graphene nanoribbons, *Nature* **444**, 347 (2006).
  - [81] X. Li, X. Wang, L. Zhang, S. Lee, and H. Dai, Chemically derived, ultrasmooth graphene nanoribbon semiconductors, *science* **319**, 1229 (2008).
  - [82] L. Jiao, L. Zhang, X. Wang, G. Diankov, and H. Dai, Narrow graphene nanoribbons from carbon nanotubes, *Nature* **458**, 877 (2009).
  - [83] J. Cai, P. Ruffieux, R. Jaafar, M. Bieri, T. Braun, S. Blankenburg, M. Muoth, A. P. Seitsonen, M. Saleh, X. Feng, *et al.*, Atomically precise bottom-up fabrication of graphene nanoribbons, *Nature* **466**, 470 (2010).
  - [84] K. Nakada, M. Fujita, G. Dresselhaus, and M. S. Dresselhaus, Edge state in graphene ribbons: Nanometer size effect and edge shape dependence, *Physical Review B* **54**, 17954 (1996).
  - [85] R. Eissele, B. B. Roy, S. Tewari, and T. D. Stanescu, Topological invariant for finite systems in the presence of disorder, arXiv preprint arXiv:2508.13146 (2025).